Master of Science Dissertation:

# A study of susceptibility-weighted MRI including a comparison of two different implementations

Stefanie Eriksson

Supervisor:

Karin Markenroth Bloch

Department of Medical Radiation Physics, Clinical Sciences, Lund
Lund University, Lund Sweden, spring 2011

# Abstract

Susceptibility Weighted Imaging is an MRI- and post-processing technique that utilize the phase information from the MR signal to enhance the contrast in areas with different susceptibility than surrounding tissue in T2*-weighted images. This technique is becoming more and more important as a clinical tool. Susceptibility-weighted imaging has been commercialized by Siemens Healthcare under the acronym SWI. As of recently, Philips Healthcare offers the beta-version of a post-processing technique for susceptibility-weighting called PADRE (Phase difference Enhanced). The post-processing steps of PADRE have not yet been published.

Phantom experiment and volunteer studies were made to compare the two techniques qualitatively and quantitatively. A MATLAB program for SWI was written and the influence of different parameters used in acquisition and post-processing for SWI and PADRE was evaluated by quantifying contrast in the images.

Differences in post-processing between SWI and PADRE were shown by comparing the results of the implementations with the post-processing result of the MATLAB SWI program. Some differences in overall image quality and in contrast between the two techniques, as well as between two different pulse sequences used, were found. Contrast enhancement was shown to be higher for PADRE than for SWI in the phantom experiments. However, no significant difference between the two implementations could be shown when measuring CNR enhancement in a large number of veins in healthy volunteers.

Popularized smmury in Swedish

# Magnetiskt blod ger kontrast i bilder av hjärnan

**Med hjälp av en MR-kamera (magnetresonans-kamera) kan skiktbilder av kroppens inre skapas. Kroppens vävnader har olika magnetiska egenskaper och kan i skiktbilden ge antingen stark eller svag signal. Detta skapar kontrast i MR-bilden och kan hjälpa läkaren att diagnostisera eventuella sjukdomar och skador. En magnetisk egenskap som kan användas för att skapa bildkontrast är *susceptibilitet*, även kallad "magnetiserbarhet". I detta arbete undersöktes funktionen av susceptibilitetsviktad MR. Speciellt studerades synbarheten hos vener i hjärnan och det gjordes en jämförelse mellan två olika leverantörers implementeringar av tekniken.**

Bilder av kroppens inre utnyttjas i stor omfattning inom sjukvården. En bildgivande teknik som används för att generera bilder av mjukvävnader i kroppen är MR. För denna teknik används en mycket stark magnet, vars magnetfält påverkar kärnorna i kroppens väteatomer. Inuti MR-kameran sätts en spole runt den kroppsdel som ska undersökas. Spolen sänder ut radiovågor som påverkar vätekärnorna. Dessa skickar tillbaka en signal som kan mätas. Olika vävnader har olika magnetiska egenskaper. Beroende på hur bildutläsning görs, det vill säga hur inställningarna är satta på MR-kameran, kan bilderna *viktas* på olika sätt. Viktning innebär att olika vävnader kan ge antingen stark eller svag signal, och det uppstår kontrast i MR-bilden.

En vävnadsspecifik egenskap som kan utnyttjas för att skapa kontrast i bilderna är *susceptibilitet*, som beskriver hur magnetiskt ett material blir i ett yttre magnetiskt fält. Susceptibiliteten hos ett material kan antingen vara negativ, positiv eller noll. En negativ susceptibilitet försvagar det yttre magnetfältet, medan en positiv susceptibilitet förstärker det yttre magnetfältet. Susceptibilitetsskillnader mellan olika vävnader kommer därför att orsaka störningar i magnetfältet. I en så kallad T2*-viktad bild kommer störningar i magnetfältet att orsaka signalminskning, vilket visar sig som mörka områden i bilden. Störningar i magnetfältet kommer inte bara att påverka storleken på signalen, utan även den så kallade fasen hos signalen påverkas. I en fasbild kan man se hur magnetfältet varierar inuti kroppen.

Vid susceptibilitetsviktad bildtagning kombineras den T2*-viktade bilden med information från fasbilden för att ytterligare öka kontrasten i områden med annan susceptibilitet än omgivningen. Ett exempel på ett sådant område är vener, det vill säga blodkärl som innehåller syrefattigt blod. Det syrefattiga blodet i venerna har högre susceptibilitet än omgivande vävnad och kan därför göras synligt med susceptibilitets-viktad MR.

I detta arbete har kontrasten för vener i hjärnan undersökts i susceptibilitetsviktade bilder. Venkontrastens påverkan av utläsningsparametrar och efterbearbetning av bilderna har studerats. Dessutom har en jämförelse mellan två olika MR-kameratillverkares implementering gjorts. Det visade sig att det finns många olika parametrar som påverkar hur stor kontrastförstärkningen i den susceptibilitetsviktade bilden blir och att det finns en del skillnader mellan de två kameratillverkarnas implementeringar.

# Abbreviations

| | |
|---|---|
| 2D | Two-dimensional |
| 3D | Three-dimensional |
| AP | Anterior-posterior |
| AR | Aspect ratio |
| CNR | Contrast to noise ratio |
| CSF | Cerebrospinal fluid |
| GRE | Gradient echo |
| HF | Head-feet |
| minIP | minimum intensity projection |
| MRI | Magnetic resonance imaging |
| NEMA | National Electrical Manufacturers Association |
| PADRE | Phase difference enhanced imaging |
| PD | Proton density |
| PRESTO | Principles of echo-shifting with a Train of Observations |
| PRIDE | Philips Research Image-processing Development Environment |
| RF | Resonance frequency |
| RL | Right-left |
| ROI | Region of interest |
| SENSE | Sensitive encoding |
| SD | Standard deviation |
| SNR | Signal to noise ratio |
| SWI | Susceptibility-weighted imaging |
| $T_E$ | Echo time |
| TE | Tissue-enhancement mode |
| VE | Vessel-enhancement mode |

# Table of contents


**Introduction** ..... 5
**Theory** ..... 6
**Background** ..... 6
Susceptibility and phase ..... 6
The phase image ..... 7
Field changes due to susceptibility in an infinite cylinder ..... 8
Susceptibility in the human body ..... 10
**Susceptibility Weighted Imaging** ..... 11
Gradient echo pulse sequence and MR signal ..... 11
Phase filtering ..... 11
Creating the phase mask ..... 12
Phase mask multiplication ..... 13
Minimum intensity projection ..... 14
Voxel aspect ratio ..... 14
**Materials and methods** ..... 15
**Pulse sequences** ..... 15
**Post-processing techniques** ..... 16
SWI on the Siemens system ..... 16
PADRE on the Philips system ..... 16
MATLAB SWI program ..... 18
**Measurements** ..... 18
Contrast measurements ..... 18
Noise measurements ..... 19
**Phantom experiments** ..... 21
Phase mask dependence ..... 21
Contrast as a function of filter size ..... 22
Contrast as a function of cylinder size ..... 22
CNR as a function of m ..... 22
**Volunteer studies** ..... 23
CNR enhancement measurements ..... 23
Voxel aspect ratio in sagittal images ..... 24
**Patient images** ..... 25
**Results** ..... 25
**Phantom experiments** ..... 25
Phase mask dependence ..... 25
Contrast as a function of filter size ..... 28
Contrast as a function of cylinder size ..... 29
CNR as a function of m ..... 30
**Volunteer studies** ..... 31
CNR enhancement measurements ..... 32
Voxel aspect ratio in sagittal images ..... 33
**Patient images** ..... 35
**Discussion** ..... 36
**Phantom experiments** ..... 36
**Volunteer studies** ..... 37
**Patient images** ..... 38
**Methods** ..... 39
**Conclusions** ..... 40
**Future work** ..... 41
**Acknowledgments** ..... 41
**References** ..... 42
**Appendix** ..... 44
**Phase sign convention** ..... 44

# Introduction

Magnetic resonance imaging is a technique where a high magnetic field is utilized to affect the hydrogen nuclei, which possess magnetic spin, to create a net magnetization. This magnetization can be measured and quantified by application of a series of RF pulses, what is called a pulse sequence. Depending on the different magnetic properties of various tissues in the body, the properties of the measured signal will vary and contrast will appear. The established method is using the magnitude of the signal for image formation, resulting in what is called the magnitude image. The most common magnetic properties that are utilized for creating contrast in MR images are relaxation times, such as T1, T2 and T2* as well as the amount of water in tissue (proton density, PD). Another magnetic property of tissues that can be utilized for image contrast is magnetic susceptibility. If the susceptibility within an object varies, then the magnetic field within the object will vary as well. This will influence the phase of the local MR signal, which is dependent of the strength of the magnetic field. Therefore, the phase image can give information about the susceptibility in an object and thus can be used to create contrast in MR images.

Susceptibility Weighted Imaging is an MRI-technique that can enhance image contrast in areas where the magnetic susceptibility in a tissue differs from the susceptibility in neighbouring tissues. The image contrast in the magnitude image is acquired by using a T2*-weighted gradient echo pulse sequence. Further contrast enhancement is achieved by using the phase image to create a so called phase mask. The pixels of the phase mask are assigned a value either somewhere between zero and one or exactly one, depending on whether the phase is positive or negative. When the phase mask is multiplied with the magnitude image, the signal intensity is consequently reduced in areas with a specific phase sign.

Susceptibility weighting imaging is becoming more and more important as a clinical tool, since the resulting image gives excellent contrast between deoxygenated blood in veins and grey or white matter. It can also give additional diagnostic information about pathologies associated with many different neurological diseases. Examples of such pathologies are: microbleeds, iron deposits, vascular malformations and calcifications [1].

SWI (Susceptibility Weighted Imaging) is a contrast enhancing technique which was developed by Haacke *et al.* [2] and has been commercialized by Siemens Healthcare. Recently, Philips Healthcare has developed a somewhat different technique for susceptibility weighted MRI, called PADRE (Phase Difference Enhanced Imaging)[3].

Siemens and Philips are the MR scanners available at Lund University hospital[1] [4]. In this work the two different techniques mentioned above, will be compared; image acquisition, post-processing and image quality will be studied and evaluated.

The part of this work concerned with image acquisition attempts to show how different parameters, used in acquisition and post-processing for SWI and PADRE, influence the final images. To do this, measurements on phantoms and volunteers have been executed on both MR systems. Investigation of post-processing has been done using the vendor supplied tools as well as a program developed specially for this work. Furthermore, image examples of a clinical patient, examined with both techniques, will be presented.

[1] General Electric MRI scanners provide a pulse sequence for susceptibility weighted imaging called SWAN (Susceptibility Weighted Angiography). This technique does not utilize any phase information and it will not be investigated further in this work.

# Theory

## *Background*

### Susceptibility and phase

The magnetic property of tissue and other elements that can be present in the human body is of great importance in magnetic resonance imaging. Magnetic susceptibility, $\chi$, is a material property that describes the magnetization, $\vec{M}$, of the material in an outer magnetic field, $\vec{H}$. For linear materials this relation follows

$$\vec{M} = \chi \vec{H} . \qquad \text{Eq. 1}$$

If the susceptibility for a material is larger than zero, $\chi > 0$, it is called paramagnetic. Paramagnetism arises when the material contains atoms with unpaired electrons. The unpaired electrons produce nonvanishing permanent magnetic moments which are randomly distributed in the absence of a magnetic field. When these magnetic moments experience an external magnetic field they produce a bulk magnetic moment, augmenting the external field within the material. The paramagnetic effect is temperature dependent, being stronger at lower temperatures.

The orbital motion of electrons around atoms will be modified in an applied magnetic field. This will, in accordance with Lenz's law, create a magnetic field opposite to the applied field. This mechanism happens in all materials and is called diamagnetism. Diamagnetism is much weaker than the paramagnetic effect. If there is no or very little paramagnetic effect in a substance then the resultant susceptibility will be diamagnetic, $\chi < 0$.

Ferromagnetism arises when a material consists of small domains, each of which is magnetized already in the absence of an external field. The susceptibility of ferromagnetic materials is greater than 0, and several orders of magnitude larger than for paramagnetic substances. In the following, we only discuss diamagnetic and paramagnetic substances.

The relationship between the magnetic field, $\vec{B}$, inside an isotropic material where no specific directions are designated, and the outer magnetic field, $\vec{H}$, is parallel and linear, with permeability, $\mu$, as the proportionality constant

$$\vec{B} = \mu \vec{H} \qquad \text{Eq. 2}$$

The susceptibility is related to the permeability of the material in the following way:

$$\chi = \frac{\mu}{\mu_0} - 1 \qquad \text{Eq. 3}$$

where $\mu_0 = 4\pi \cdot 10^{-7}$ is the permeability of vacuum. It can now be shown [5, 6] that the resultant magnetic field, $\vec{B}$, inside an isotropic object with the susceptibility, $\chi$, and the magnetization, $\vec{M}$, is

$$\vec{B} = \frac{1+\chi}{\chi}\mu_0 \vec{M}(\chi) \qquad \text{Eq. 4}$$

When the magnetic field inside an object varies spatially as a result of the differences in susceptibility, it will influence the phase of the MR signal, which will vary spatially in the same way. The measured phase, $\varphi$, is proportional to the change in the magnetic field, $\Delta B = B - B_0$ where $B$ is the magnetic field in the object and $B_0$ is the external applied magnetic field. The measured phase is also proportional to the echo time, $T_E$. The expression for the phase is

$$\varphi = -\gamma \Delta B T_E \qquad \text{Eq. 5}$$

where $\gamma = 42.6\,\text{MHz/T}$ is the gyro-magnetic ratio for $^1$H. The change in the magnetic field, $\Delta B$, is not only a function of susceptibility, $\chi$, but it is also dependent on geometrical factors, such as size, shape and direction.

**The phase image**

The MR signal is generally described as a complex signal with a real and an imaginary part. This complex signal can be written as

$$\hat{\rho} = \text{Re} + i\,\text{Im} \qquad \text{Eq. 6}$$

or as

$$\hat{\rho} = \rho_m e^{i\varphi} \qquad \text{Eq. 7}$$

where $\rho_m$ is the magnitude of the signal and $\varphi$ is the phase of the signal. An illustration of the MR signal is shown in Figure 1.

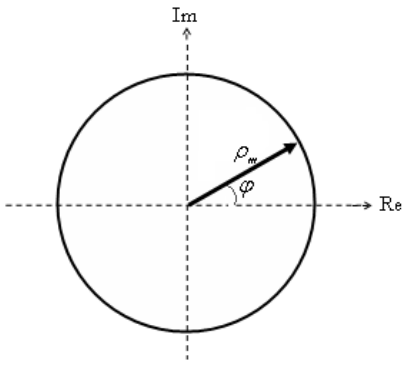


**Figure 1.** Illustration of the MR signal as a complex number.

The phase image $\varphi(x, y)$ is obtained by calculating the argument of the complex signal as follows

$$\varphi(x, y) \equiv Arg\ \hat{\rho}(x, y) = \tan^{-1}\left(\frac{\mathrm{Im}\ \hat{\rho}(x, y)}{\mathrm{Re}\,\rho(x, y)}\right). \qquad \text{Eq. 8}$$

The phase values lie within the interval $[-\pi, \pi)$ and the pixels in the phase image can only take on values within this interval, although the true phase value might take on any real value. When the true phase values of the spins are differing with more than $2\pi$, it will result in phase aliasing, also called phase wraps, in the phase image. An example of this is shown in Figure 2 where pixels with the same intensity have phase values that differ by multiples of $2\pi$.

**Figure 2.** Example of a phase image. The pixel values in the image are restricted between $-\pi$ and $\pi$, creating phase wraps where the highest intensity goes directly to the lowest intensity as the phase value goes from $+\pi$ to $-\pi$.

If the magnetic field was homogeneous in the whole object, the phase would be equal everywhere in the phase image. This is usually not the case as both macroscopic and microscopic field changes influence the phase of the MR signal. In this case, macroscopic variations refer to field changes across the whole object, which can result from an inhomogeneous external main magnetic field, $B_0$. The microscopic field changes appear in smaller regions and can be due to differences in susceptibility between neighbouring tissues.

**Field changes due to susceptibility in an infinite cylinder**

Blood vessels can be modeled as circular cylinders with constant susceptibility. If we consider an infinite cylinder with an inner susceptibility, $\chi_{in}$, that differs $\Delta\chi$ from the outer susceptibility, $\chi_{out}$, ($\Delta\chi = \chi_{in} - \chi_{out}$), the inner and outer magnetic field, $\vec{B}_{in}$ and $\vec{B}_{out}$, will depend on what angle the axis of the cylinder has against the direction of the magnetic field, $B_0$.

As a first approximation, assume that the cylinder axis is along the z-direction, parallel to the main magnetic field, $\vec{B}_0 = B_0\hat{z}$. The field outside of the cylinder, $\vec{B}_{out}$, will in this case be equal to the main field *i.e.* the change in the magnetic field will be zero, $\Delta\vec{B}_{out} = 0$. The change in the field inside the cylinder will be $\Delta\vec{B}_{in} = \Delta\chi\vec{B}_0$ [5].

If, on the other hand, the cylinder axis is along the x-direction, perpendicular to $B_0$, the change of the magnetic field inside of the cylinder will be

$$\Delta\vec{B}_{in} = \frac{\Delta\chi/2}{1+\Delta\chi/2} B_0 \qquad \text{Eq. 9}$$

[5, 7].

The field outside of the cylinder perpendicular to the main magnetic field can be described in cylindrical coordinates and will vary as

$$\Delta\vec{B}_{out} = \frac{\Delta\chi/2}{1+\Delta\chi/2}\left(\frac{a}{\rho}\right)^2 \cos 2\phi \cdot B_0 \qquad \text{Eq. 10}$$

where $a$ is the radius of the cylinder, $\rho$ is the distance from the cylinder axis and $\phi$ is the angular coordinate [5, 7]. The general expressions for the field changes inside and around the cylinder depending on the angle $\theta$, between the cylinder axis and the main magnetic field (see Figure 3), are

$$\Delta\vec{B}_{in} = \frac{\Delta\chi}{2} B_0 (1+\cos^2\theta) \qquad \text{Eq. 11}$$

$$\Delta\vec{B}_{out} = \frac{\Delta\chi}{2} B_0 \sin^2\theta \left(\frac{a}{\rho}\right)^2 \cos 2\phi \qquad \text{Eq. 12}$$

[5].

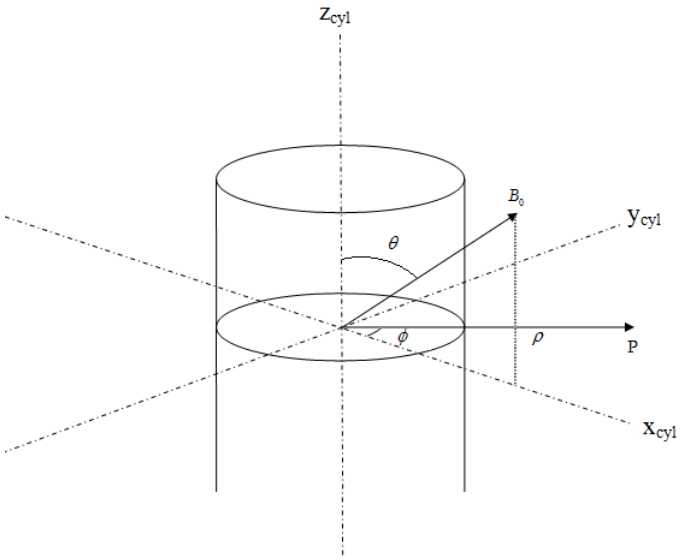


**Figure 3.** Cylinder coordinates describing the point P outside of a cylinder. The cylinder is positioned with the cylinder axis at an angle $\theta$ against $B_0$. The Cartesian coordinates of the cylinder ($x_{cyl}$, $y_{cyl}$, $z_{cyl}$) is also shown, with the coordinate $z_{cyl}$ representing the cylinder axis, and the $x_{cyl}$ coordinate representing the projection of $B_0$ onto the cross-section of the cylinder. $\phi$ is the angle between P and the $x_{cyl}$-axis. (Image borrowed and modified [5])

The above equations are valid if the susceptibility is assumed to be very small, $|\chi| << 1$, which is the case in human tissue. Furthermore, the above equations assume materials of continuous magnetizations, and do thus not hold for individual spins. To account for the cancellation of fields due to neighboring molecules, the so called Lorentz correction is added to the equations for the change in the magnetic field. When the Lorentz correction is included, the general equation for the magnetic field shift inside and outside of a cylinder with an angle, $\theta$, to the external magnetic field, $B_0$, is given by

$$\Delta B_{in} = \frac{\Delta\chi}{6}(3\cos^2\theta - 1)B_0 + \frac{1}{3}\chi_{out}B_0 \qquad \text{Eq. 13}$$

$$\Delta B_{out} = \frac{\Delta\chi}{2}\frac{a^2}{\rho^2}\sin^2\theta\cos 2\phi \cdot B_0 + \frac{1}{3}\chi_{out}B_0 \qquad \text{Eq. 14}$$

According to Eq. 13, the field shift inside the cylinder will be zero if the angle $\theta$ is about 55° which is referred to the magic angle [8].

As a consequence of the angular dependence of the external field on $\phi$ (Eq. 14) the resulting magnetic field around a cylinder perpendicular to the magnetic field will get a flower shaped appearance. As is shown in Figure 4 the magnetic field shift is positive in the direction parallel to the magnetic field and negative in the direction perpendicular to the magnetic field. At the angle $\phi$ =45° from the main magnetic field, shown in the picture by the straight lines, the magnetic field shift is zero.

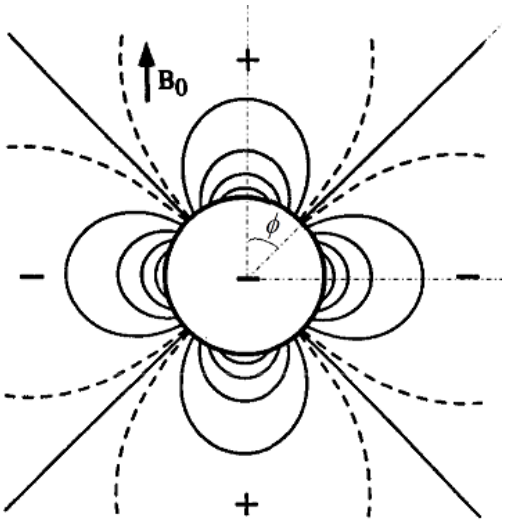


**Figure 4.** Cross section of cylinder perpendicular to the main magnetic field, showing field shift signs. The angle $\phi = 45°$ is marked to show where the field shift is zero. (Image borrowed and modified [7])

**Susceptibility in the human body**

Human tissues are diamagnetic with susceptibilities close to that for water which is the main component in the body. Other components are of such low concentration that the changes in susceptibility between different tissues are just some fractional parts per million (ppm). The susceptibility in water at 37 °C is approximately $-9.05 \cdot 10^{-6}$ [7].

In blood, oxygen is carried by hemoglobin to the cells in the body. Hemoglobin consists of four protein subunits each containing one iron ion, $Fe^{++}$. This ion is paramagnetic as it contains two unpaired electrons. When the iron ion binds to oxygen, which also has unpaired electrons, it results in an oxyhemoglobin molecule with no unpaired electrons. Oxyhemoglobin is slightly more diamagnetic than water. When the oxygen is transferred to the cells the remaining deoxygenated hemoglobin possesses four unpaired electrons and is thus paramagnetic. As a result of the different magnetic properties of hemoglobin, blood can either be diamagnetic relative to the surrounding tissue, as in fully oxygenated blood in arteries, or paramagnetic relative to the surrounding tissue, as in deoxygenated blood in veins. The resultant susceptibility in venous blood depends on the oxygen saturation and the hematocrit, which is the fraction of red blood cells in the blood. The difference in susceptibility between fully deoxygenated blood cells and fully oxygenated blood cells is 0.27 ppm [9].

Further oxidization of deoxyhemoglobin takes place in for example haemorrhages, the product is called methemoglobin and possesses five unpaired electrons. Haemorrhages is therefor also a source of paramagnetic changes of susceptibility [1].

There are other sources of varied susceptibilities in the human body such as non-heme iron and calcium. Iron accumulations, which are paramagnetic, have been associated with some neurodegenerative diseases [1, 10, 11]. Calcifications can be differentiated from haemorrhages because calcium is diamagnetic [10].

## *Susceptibility Weighted Imaging*

Susceptibility Weighted Imaging (SWI), developed by Haacke *et al.* [2], is an acquisition and post-processing technique that utilizes phase information to enhance contrast in areas with different susceptibility compared to the background. SWI has been shown to give additional diagnostic information about different neurological disorders such as: stroke, haemorrhages, tumours, vascular malformations, traumatic brain injuries and neurodegenerative disorders [11-14].

### Gradient echo pulse sequence and MR signal

The SWI processing uses magnitude and phase images from a high resolution, three dimensional, gradient echo pulse sequence. A gradient echo sequence uses gradients to refocus spins to an echo. Because of inhomogenities in the magnetic fields, spins will dephase faster and the refocusing at the time of the echo will be incomplete. This is referred to as T2*-relaxation and causes a lowering of the MR signal. Variations in susceptibility will result in magnetic field distortions and such areas will thus have shorter T2*-relaxation times, and will be seen as hypointense areas in the magnitude image. As mentioned above, the phase of the MR signal is also dependent on susceptibility. A gradient echo sequence with relatively long echo time, $T_E$, will therefore give a T2*-weighting, which is partly a susceptibility weighting.

A spin echo sequence rephases the T2*-effect, and is thus not useful for generating susceptibility weighted images.

### Phase filtering

In conventional MRI, only information in the magnitude of the signal is used for image formation. The phase image gives additional information about the magnetic field variations in the measured object.

However, the phase information contains both microscopic and macroscopic field changes. The microscopic field changes gives information about the susceptibility variations in the object. The macroscopic field changes are due to background inhomogeneities in the external magnetic field, causing low spatial frequency phase variation over the object [8]. The macroscopic phase variations do not contain information useful for SWI. To get rid of this macroscopic field information, the phase image is high-pass filtrated [1, 6, 8]. The high-pass filtration is performed on the unwrapped phase images. This is usually done by a so-called homodyne-filtration where a low pass two-dimensional Hanning filter is applied to the original k-space data [8].

The Hanning filter is basically the Hann function (Eq. 15) in two dimensions. The Hann function is given by

$$w(n) = 0.5\left(1 - \cos\left(\frac{2\pi n}{N-1}\right)\right) \qquad \text{Eq. 15}$$

where N is the width of the function and $n$ is an integer with values $0 \le n \le N-1$ [15]. The Hann function is illustrated in Figure 5.

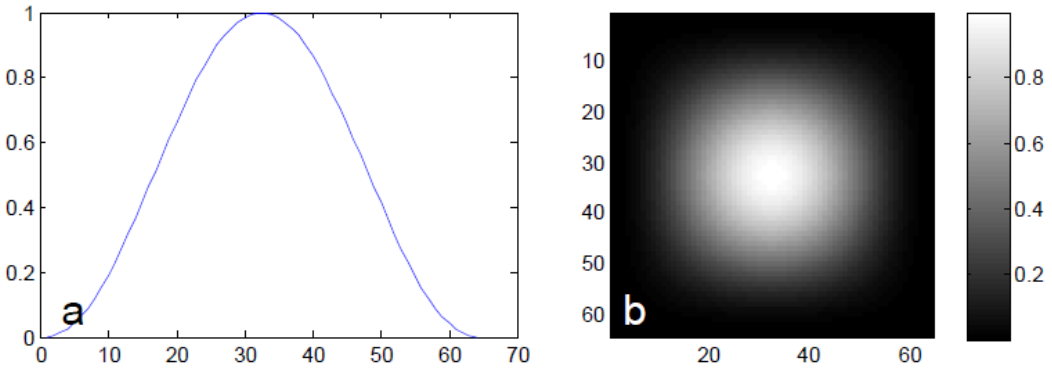


**Figure 5**. Hann functions in (a) one dimension and (b) two dimensions of sizes 64 and 64x64 respectively. The 2D Hann function is used as a filter. The low-pass filter is applied to the k-space data. When the original k-space data is complex divided with the low-pass filtrated data, removing the background phase variations that causes wraps in the phase image, a high-pass filter effect arises.

To get rid of the macroscopic field inhomogenities from the phase image, the original k-space data is complex divided by the low pass filtered data leaving only microscopic field phase information [6, 8, 16]. The filter size is an important parameter in the SWI processing. A too small filter will not clear all of the macroscopic field inhomogenities while a too large filter will remove too much of the microscopic field inhomogenities. As an example, Wang *et al. [8]* demonstrated elimination of the low spatial components of the phase in a 256x256 matrix image using a Hanning filter with the filter size 32x32.

### Creating the phase mask

From the filtered phase image a so-called phase mask is created. The phase mask is designed to further decrease the signal for pixels with a certain phase sign. A phase mask takes on values between zero and one. To generate a negative phase mask, $f_{\text{negative}}(x,y)$, positive phase values are set to unity and negative phases are set to a value between zero and one according to the following equation:

$$f_{negative}(x, y) = \begin{cases} (\varphi(x, y) + \pi)/\pi, & \varphi(x, y) < 0 \\ 1, & \varphi(x, y) \geq 0 \end{cases} \quad \text{Eq. 16}$$

For a positive phase mask, $f_{positive}(x,y)$, the opposite approach is taken so that all negative phase values are set to unity while all positive phase values are set to a value between zero and one, according to:

$$f_{positive}(x, y) = \begin{cases} (\pi - \varphi(x, y))/\pi, & \varphi(x, y) > 0 \\ 1, & \varphi(x, y) \leq 0 \end{cases} \quad \text{Eq. 17}$$

In SWI, the negative phase mask is used to enhance the contrast for the veins. The reason that a negative phase mask is suitable is the voxel aspect ratio used, this will be further explained below [1, 17, 18]. See also the Appendix for definitions of the phase sign conventions.

**Phase mask multiplication**

When the phase mask has been created it will be multiplied with the magnitude image several times. The number of multiplications is usually four, which has been shown by Haacke *et al.*. [2] to give good contrast to noise ratio (CNR) without adding excessive noise to the image. In the negative phase mask case, pixels with negative phase will be suppressed. Pixels with the most negative phase, $-\pi$, will be completely nulled and less negative phases will be partially suppressed. Pixels with positive phase values will not be affected by the negative phase mask. The resulting image will thus be hypointense in regions where the phase is negative. The different images and post-processing steps used for creating an SWI image are shown in Figure 6. The number of multiplications with the phase mask is represented by the variable *m*.

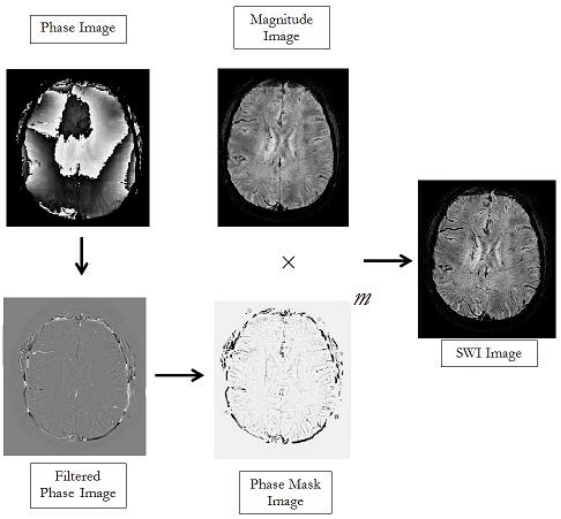


**Figure 6.** Post-processing steps for creating an SWI image. The phase image (top left) is first filtered to remove macroscopic phase variations. A phase mask is created from the filtered phase image. The phase mask is multiplied *m* times with the magnitude image to create the SWI Image.

### Minimum intensity projection

To visualize the vascular formations inside the brain, a minimum intensity projection (minIP) is often made. This processing technique is useful to review the venous configuration in SWI images. The minIP projects the lowest intensity along one direction in a slab of multiple slices. The thickness of the slab can be varied. A thick slab can give a better overview of more vessels in one slice, and a thin slab gives a better vessel localization [19]. The minIP on SWI is normally done in a transversal direction, *i.e.* the projection angle is the same as the slice direction. Examples of a normal SWI and a minIP SWI are shown in Figure 8c and Figure 8d.

### Voxel aspect ratio

When visualising veins with the SWI method, the resolution is of great importance. Veins are usually smaller than the voxels used in MRI, and therefore the voxels will contain two compartments with both the vein and the surrounding parenchyma [1, 17, 18].

As was shown in the section *Field changes due to susceptibility in an infinite cylinder*, there will be areas of negative as well as positive magnetic field shifts around a vessel that is perpendicular to the main magnetic field, see Figure 4. The measured phase value in a voxel will depend on how much of the different areas of field shifts that are included in the voxel [1].

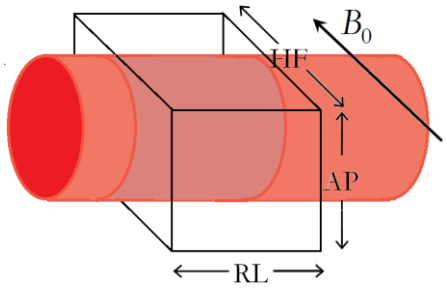


**Figure 7.** Voxel with the aspect ratio RL/AP/HF, containing two compartments: vein and parenchyma. For transversal images of the brain, the HF length is the same as the slice thickness. To enhance the vessel contrast, the AR should be such that the voxel dimensions parallel to the magnetic field is at least twice as long as the voxel dimensions perpendicular to the magnetic field [17, 18].

When the negative phase mask is used, the voxels must have aspect ratios, AR, so that they include more negative phases than positive phases around a vessel, or else the positive and negative phases in the voxel will cancel each other. If the aim is to visualize in-plane veins in transversal slices of the brain with SWI the optimal aspect ratio of RL/AP/HF has been shown to be such that the HF length is at least twice as long as the RL and AP lengths [17, 18], where RL is the right-left voxel width, AP is the anterior-posterior voxel height and HF is the head-feet voxel depth. In transversal images, HF is the same as the slice thickness, and has the same direction as the main magnetic field, see Figure 7.

# Materials and methods

All measurements in this study were done on the two different 3T MR systems that are stationed at Lund University Hospital: Siemens Skyra 3T MRI system with a 20-channel head coil, and Philips Achieva 3T MRI system with an 8-channel head coil. Susceptibility weighted post-processing was done automatically on the Siemens system when using the SWI sequence. On the Philips system the beta program PADRE PRIDE tool was used. The post-processing in PADRE PRIDE could be automatized and done directly after acquisition on the scanner, or it could be done offline.

On both the MR systems, DICOM magnitude and phase images from the gradient echo sequence were exported for offline storage. SWI post-processing was also performed using custom made MATLAB[2] scripts, using the exported magnitude and phase images from the MR scanners.

## *Pulse sequences*

To create the susceptibility weighted images, both magnitude and phase images were needed. Phase information is always internally available to the reconstruction unit, even if it is not ordinarily presented to the user. The pulse sequences used for susceptibility weighted imaging are T2*-weighted and have high resolution, while obeying the voxel aspect ratios discussed previously.

The SWI sequence used on the Siemens system is a three dimensional (3D), fully velocity compensated, gradient echo sequence. The resolution can be adjusted in any direction but this work used the resolution preset on the camera, which is also the one used clinically.

The PADRE sequence used as input to the post-processing tool on the Philips camera is a 3D PRESTO (Principles of echo-shifting with a Train of Observations) sequence [20].

**Table 1.** Pulse sequences used on respective system. The Siemens parameters were provided at the camera for clinical use. The Philips parameters were recommended by Philips healthcare [correspondence with Elizabeth Moore].

| ***Parameters*** | ***MR system*** | |
|---|---|---|
| | **Siemens** | **Philips** |
| Pulse sequence | 3D Gradient echo | 3D PRESTO |
| Echo time | 20 ms | 46 ms |
| Repetition time | 27 ms | 29 ms |
| Flip angle | 15° | 10° |
| Resolution | 0.9 x 0.9 x 1.5 $mm^3$ | 0.45 x 0.45 x 1.0 $mm^3$ |
| Field of View | 172.5 x 230 $mm^2$ | 172.5 x 230 $mm^2$ |
| Number of slices | 112 | 110 |
| Acquisition time | 05:35 | 05:28 |
| Flow compensation | Yes | No |

The resolutions and parameters used on the two different systems are shown in Table 1. The parameters in the Siemens pulse sequence is the sequence provided at the Siemens system in the clinic. The parameters in the Philips pulse sequence are according to recommendations from Philips [correspondence

[2] MATLAB R2009b, The MathWorks inc., Natick, MA

with Elizabeth Moore, Senior Clinical Scientist, Philips MR]. The main difference between the two sequences is the difference in echo time, but also resolution and flip angle differ.

On the Philips camera, two additional sequences were acquired for further comparative analysis; one gradient echo sequence with the same parameters as on the Siemens system and one PRESTO with the same resolution as the one on the Siemens system. The sequences and resolutions used on the two MR systems are presented in Table 2.

**Table 2.** The different sequences and resolutions used at the two MR scanners.

| *MR system* | *Pulse Sequence* | *Resolution* |
|---|---|---|
| Siemens | 3D Gradient echo | 0.90x0.90x1.5mm$^3$ |
| Philips | 3D PRESTO | 0.45x0.45x1.0mm$^3$ |
| Philips | 3D PRESTO | 0.90x0.90x1.5mm$^3$ |
| Philips | 3D Gradient echo | 0.90x0.90x1.5mm$^3$ |

## *Post-processing techniques*

### SWI on the Siemens system

The SWI post-processing was automatically performed on the Siemens MR system. The processing generated four different image series which are shown in Figure 8.

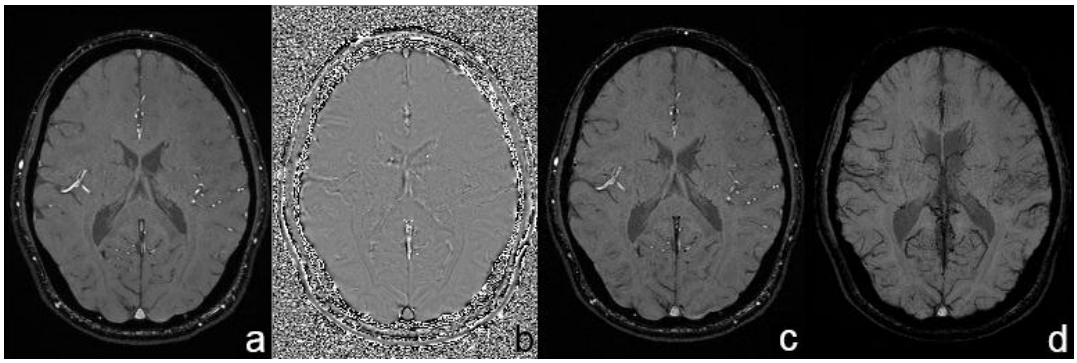


**Figure 8.** Images of a healthy volunteer scanned on the Siemens Skyra 3T system with the 3D GRE pulse sequence. The different image types generated at the Siemens camera are: (a) Magnitude image, (b) filtered phase image, (c) SWI image and (d) minIP of SWI.

### PADRE on the Philips system

The Philips scanner generates magnitude images and unfiltered phase images as shown in Figure 9. The post-processing is done using IDL-based software called PADRE PRIDE tool[3]. Post-processing can be automatically performed directly after data acquisition, or it can be done afterwards by running the program offline [3, 21].

[3] IDL 6.3,ITT Visual Information Solutions

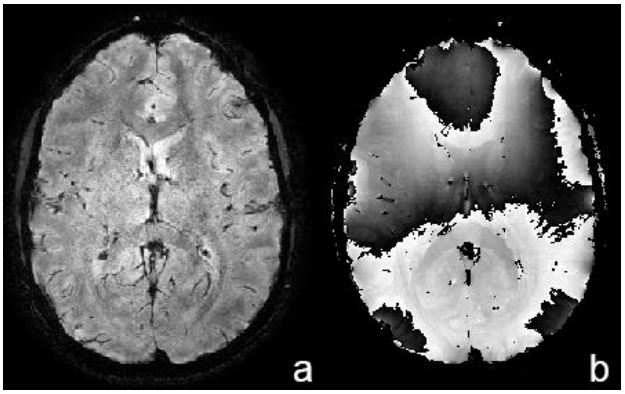


**Figure 9.** (a) Magnitude and (b) phase images of healthy volunteer scanned at the Philips MR system with a PRESTO sequence.

The software loads XML-REC files containing both magnitude and phase images. XML-REC is a native Philips image format, thus only Philips data can be processed with the PRIDE PADRE post-processing software. A brief description of the tool is given here. When the images are loaded into the PADRE PRIDE tool window it is possible to scroll through the series to see all the images. There are three different post-processing modes to choose from, they are: Vessel Enhancement (VE), Tissue Enhancement (TE) and Padre, see Figure 10. The Vessel-Enhancement mode is expected to provide good venous contrast, the Tissue-Enhancement mode enhances contrast between grey and white matter and Padre mode is a combination of both Vessel- and Tissue-enhancement mode[22] .

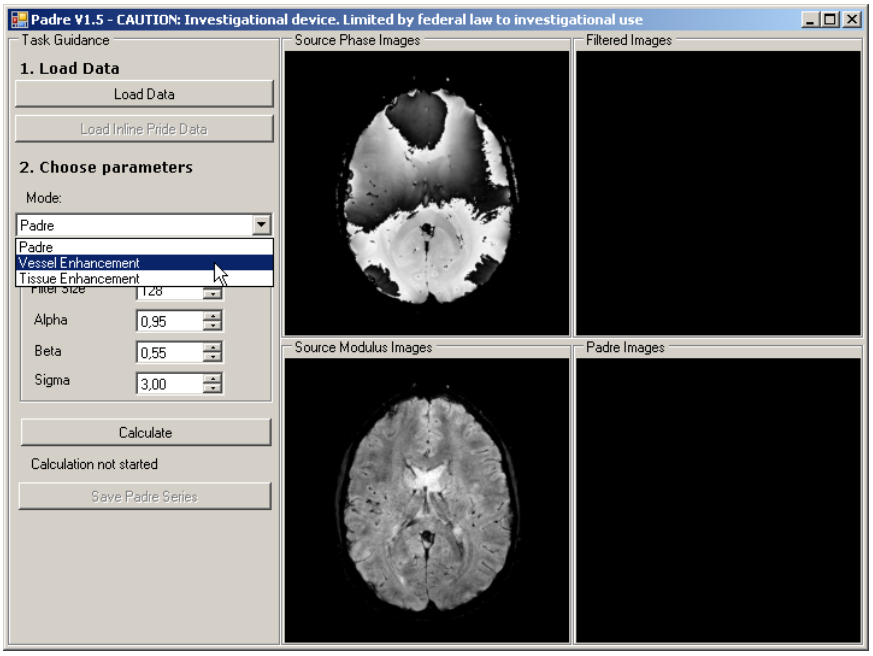


**Figure 10**. A screenshot of the PADRE PRIDE tool used for susceptibility weighted post-processing of magnitude and phase images acquired at a Philips MR system. Three different post-processing modes can be chosen in the drop down menu: Padre, Vessel Enhancement and Tissue Enhancement.

When the required post-processing mode has been selected, four other parameters can be varied, these are Filter size, Alpha, Beta and Sigma. Presently there is no documentation of what these parameters do, and

Philips recommends that the default values are used. When the parameters are set the calculation can start and the resulting images are a filtered phase image and a PADRE image, see Figure 11. The filtered phase images are not available for further use, only the PADRE images are exported.

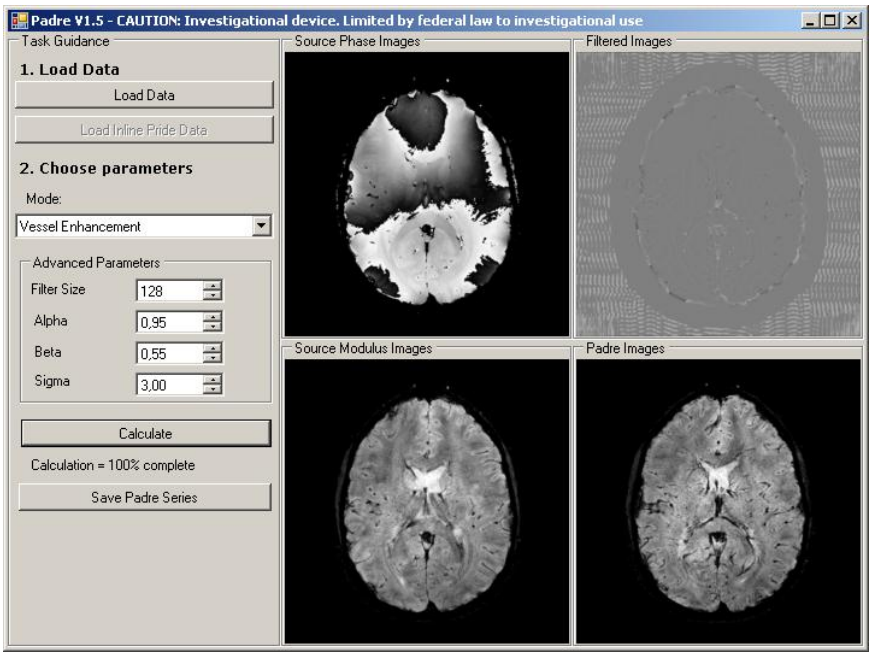


**Figure 11.** PADRE PRIDE tool window after calculation of PADRE images with Vessel Enhancement as chosen mode (lower right image). The filtered phase images are also shown (upper right image).

### MATLAB SWI program

An in-house SWI program was written using MATLAB. The program was used to make SWI images from magnitude and phase images acquired with the sequences in Table 2. SWI was done according to the procedure described in the theory section *Susceptibility Weighted Imaging*. No filtration was made on the Siemens phase images because they were already filtrated. All other steps were included except for the minimum intensity projection. This allowed for a fair comparison of how the different sequence parameters affected the SWI results.

In addition, the program included routines for the contrast measurements described below.

## *Measurements*

### Contrast measurements

To measure contrast in the images a line was drawn across the area of interest, for example a vein. A profile of the intensity along the drawn line was plotted for both the magnitude and post-processed image. Pixels of interest, representing the vein, were manually selected simultaneously in both images (see red markers in Figure 12). If more than one pixel was selected, the mean intensity value was calculated. Five pixel values on each side of the vein region were automatically marked (green markers in Figure 12b, d) and the mean of these was calculated. The contrast was then calculated by taking the difference between

the mean intensities inside and outside of the veins for the magnitude and post-processed image respectively, according to

$$Contrast = S_{out} - S_{in}. \qquad \text{Eq. 18}$$

The contrast enhancement after post-processing was then calculated by comparing the contrast in the post-processed image with the contrast in the magnitude image as follows:

$$Contrast\ enhancement = \frac{Contrast_{Post-processed} - Contrast_{Magnitude}}{Contrast_{Magnitude}}. \qquad \text{Eq. 19}$$

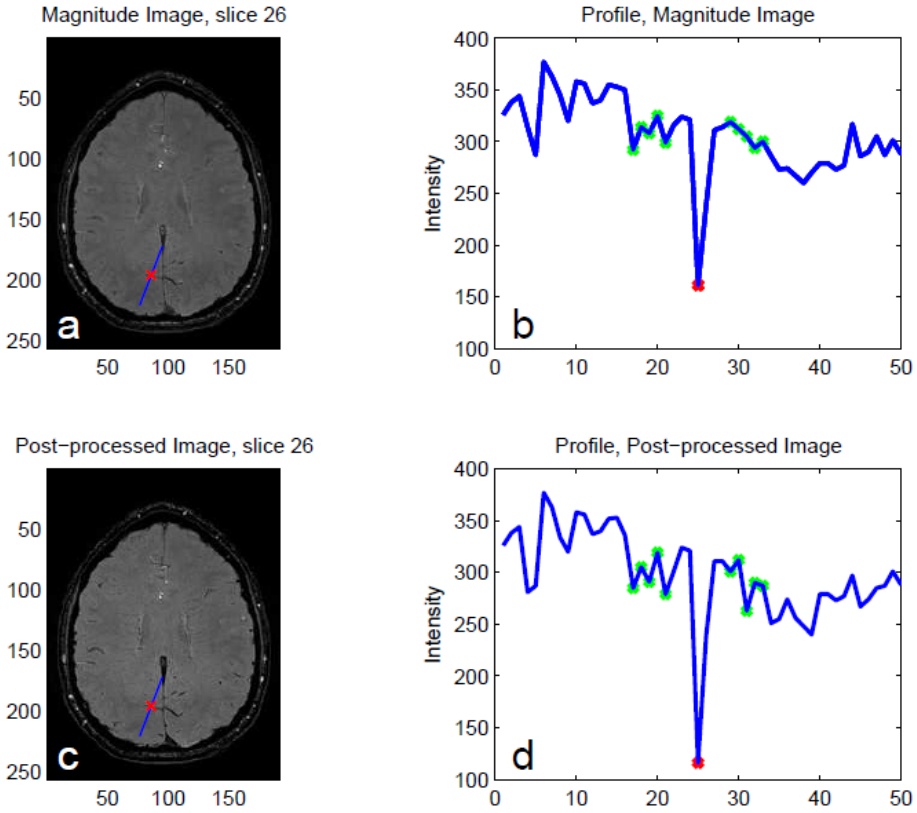


**Figure 12.** Illustration of how the contrast was measured in the images, both before and after post-processing. The red marker represents the vein pixel both in the MR images and in the intensity profiles. The green markers represent the pixels used for measuring the intensity outside of the vein.

### Noise measurements

In order to measure contrast to noise ratio, CNR, an assessment of the noise levels must be made. This is not always straightforward, especially if parallel imaging techniques are used when acquiring data. The noise in images acquired with parallel imaging is not homogenous over the image, so the noise level is position-dependent [23, 24]. In this work, three different methods of measuring noise were employed. Two of the methods are quick and do not add much scanning time during acquisition. Therefore these

noise measurements were chosen for volunteer measurements. The third method takes longer time and was therefore only used for phantom measurements.

The first method is one recommended by NEMA [25]. In this method, two images are acquired under the exact same conditions. The magnitude images are subtracted from each other and the resulting image is assumed to contain only the subtracted noise. A region of interest (ROI) is selected and the standard deviation (SD) of the pixel values within the ROI is calculated. The image noise is calculated according to

$$image\ noise = \frac{SD}{\sqrt{2}}. \qquad \text{Eq. 20}$$

The second method used is also recommended by NEMA. Two measurements are done under the exact same circumstances. The second measurement is acquired without any RF excitation and therefore contains no signal. The standard deviation is calculated for the pixels within a ROI in the signal free image and the noise is calculated according to

$$image\ noise = \sqrt{\frac{2}{4-\pi}} \cdot SD. \qquad \text{Eq. 21}$$

where the factor $\left(\sqrt{2/(4-\pi)}\right)$ corrects for the Rayleigh distribution of the noise in the magnitude image [25, 26]. The ROIs in this work were selected in the same area as the profile was drawn and they included approximately 50x50 pixels.

The third noise measurement is one of the most accurate and is based on repeated acquisitions under the same conditions. In this work, 20 such repetitions were made. The noise is determined by looking at the signal intensity of one pixel and calculating the standard deviation of the signal over time. The pixel was chosen in the same region where the outside gel intensity was measured.

$$image\ noise = SD \qquad \text{Eq. 22}$$

The three different noise measuring methods are summarized in Table 3.

**Table 3.** Short descriptions of the different noise measurements used in this work.

| ***Noise measuring method*** | ***Short description*** |
|---|---|
| 1. Difference image | A difference image is created from two identical scans and SD of the pixels within a ROI is calculated. |
| 2. No RF excitation | Two identical measurements are done, one is acquired without any RF excitation and SD is calculated within a ROI in the signal free image. |
| 3. Repeated acquisitions | 20 identical measurements are made and SD for one pixel is calculated over time. |

## *Phantom experiments*

To investigate how different parameters in the image acquisition and post-processing procedures of SWI influence the contrast in the image, two susceptibility phantoms were made. Phantom 1 consisted of four cylinders (straws and test tubes) with different diameters (3, 5, 9 and 11 mm), all aligned along the same direction, see Figure 13a. Phantom 2 consisted of three cylinders of the same diameter (5 mm), all positioned at different angles inside the phantom, see Figure 13b. The design parameters are given in Table 4. The cylinders inside the phantom were filled with agar gel containing 0.7 % agarose and 1 mM $CuSO_4$. The gel was doped with 0.1 % Gd-DTPA-BMA contrast agent. Outside of the cylinders the gel contained 0.8 % agarose and 1 mM $CuSO_4$. The gadolinium-based contrast agent was used to increase the susceptibility inside the cylinders so that it would be higher than in the outside gel. The $CuSO_4$ was used to shorten the T1-relaxation time in order to increase the MR signal from the gel. The agar was used to make the phantom solid and thus enable it to be turned and put in different directions inside the MR scanner.

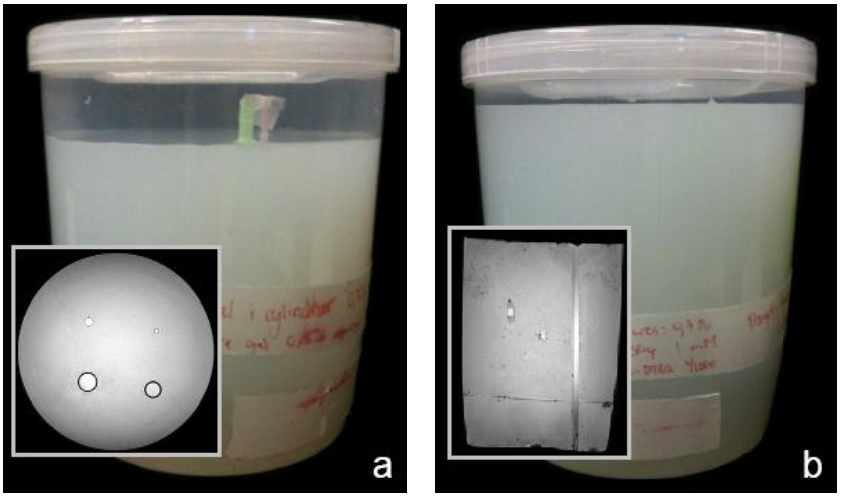


**Figure 13.** Gel phantoms with cylinders doped with gadolinium-based contrast agent. The four cylinders in the phantom to the left (a) are of different sizes (3, 5, 9 and 11 mm) and are all angled in the same direction as the axis of the phantom. A transversal MRI slice of the phantom is shown in the figure. The phantom to the right (b) contains three cylinders of the same size (5 mm) all with different angles against the axis of the phantom. A sagittal MRI slice of the phantom is shown.

**Table 4**. Design parameters for the two phantoms shown in the figure above.

| | ***Cylinder 1*** | | ***Cylinder 2*** | | ***Cylinder 3*** | | ***Cylinder 4*** | |
|---|---|---|---|---|---|---|---|---|
| | **diameter** (mm) | **angle** (°) | **diameter** (mm) | **angle** (°) | **diameter** (mm) | **angle** (°) | **diameter** (mm) | **angle** (°) |
| **Phantom 1** | 3 | 0 | 5 | 0 | 9 | 0 | 11 | 0 |
| **Phantom 2** | 5 | 0 | 5 | 49 | 5 | 90 | - | - |

### Phase mask dependence

If a positive or negative phase mask is used for SWI post-processing is naturally of great importance. To investigate how the phase mask type influences the intensity profile after post-processing for cylinders at

different angles and at different MR systems, phantom measurements were made. Phantom 1 was positioned both parallel and perpendicular to the main magnetic field and the images were post-processed with both the positive and the negative phase mask using the MATLAB SWI program. This was done at both of the MR systems.

**Contrast as a function of filter size**

Phantom 1 with different sized cylinders was scanned with the Philips system at three different angles against the static magnetic field, $\vec{B}_0$ (0°; 55° and 90°). The slice directions used during acquisition were chosen in ways that generated cross section images of the phantom, see example in Figure 13a. The sequence used was the PRESTO pulse sequence described in Table 1.

The MATLAB program was used for SWI post-processing of the images. In the post-processing, the size of the filter used for filtering the phase images where varied. Hanning filters with matrix sizes of 16x16, 32x32, 48x48, 64x64, 96x96, 128x128, 160x160, 192x192, 256x256, 384x384 were used on 512x512 matrix images. Apart from the filter size all other parameters were held constant and the post-processing were done according to standard SWI. The choice of positive or negative phase mask was made after visual inspection of the post-processed images shown in Figure 16 and Figure 17, establishing witch phase mask that generated a signal cancellation inside the cylinders. This analysis was done only for images acquired at the Philips MR system because the phase images from the Siemens camera are already filtered when presented to the user.

For the cylinders angled at 55° against the static magnetic field, both types of the phase masks were used, in two separate post-processings, to test the agreement to the theoretical phase shift at this angle, which is zero according to Eq. 5 and Eq. 11. Therefore there should be no contrast enhancement after post-processing. The contrast was measured in the same way as previously described and shown in Figure 12, but the profile lines were drawn at a 45° angle across each cylinder (see Figure 14) to avoid the field distortions outside of the cylinders.

**Contrast as a function of cylinder size**

The contrast for the different cylinder sizes in phantom 1 was measured. The phantom was positioned at different angles (0°, 90° and 55°) to the main magnetic field inside the MR camera. The sequences and resolutions in Table 2 were used. The different post-processing techniques used were SWI and PADRE on Siemens and Philips respectively. The three different modes of PADRE were all evaluated: Padre, vessel enhancement and tissue enhancement.

Contrast was measured with the same method that is described above. Comparisons were done between SWI and the PADRE post-processing modes.

**CNR as a function of *m***

CNR was measured for one cylinder in images of phantom 2 acquired with the sequences displayed in Table 1. This was done for post-processed images where various numbers of multiplications of the phase mask onto the magnitude image had been used. The post-processing was done with the MATLAB SWI program. Values of *m* were 1, 2, 4, 6, 8, 12, 16, 20, 30, 50 and 100. The filter size used for filtrating Philips phase images was 96x96. The noise measurements were done according to the three different methods

described in Table 3. On the Siemens system, method 1 and method 3 were used. On the Philips system, method 2 and 3 were used. When using method 2, the noise in the post-processed image was estimated by comparing the SD in a ROI in the magnitude and SD in the same ROI in the post-processed image. The noise in the signal free image was then calibrated according to Eq. 23 to get the noise in the post-processed image.

$$N_{Post-processed} = SD_{Post-processed} \cdot \frac{N_{Magnitude}}{SD_{Magnitude}} \quad \text{Eq. 23}$$

$N_{Magnitude}$ is the noise measured in the signal free magnitude image as in Eq. 22.

Contrast in the images was measured and the *Contrast difference* between the two images was calculated according to Eq. 24 and then the CNR was calculated according to Eq. 25 so it was actually the contrast difference to noise ratio that was measured.

$$Contrast difference = Contrast_{Magnitude} - Contrast_{Post-processed} \quad \text{Eq. 24}$$

$$CNR = \frac{Contrast\ difference}{image\ noise} \quad \text{Eq. 25}$$

where the image noise was measured in the post-processed image.

## Volunteer studies

The volunteers were examined on both MRI systems after signing a consent form. The duration between the examinations was never longer than one week. The study was approved by the local ethics committee.

The pulse sequences used were according to Table 1. Post-processing was made on respective MR system as well as with the MATLAB SWI program. The images from respective vendor were compared with regard to overall image quality and CNR enhancement.

### CNR enhancement measurements

Seven healthy volunteers were included in the study (5 males, 2 females, ages 24-59 years). The sequences and resolution used here were the ones shown in Table 1. For PADRE post-processing, the vessel-enhancement mode (VE) was used.

On the Siemens system, the difference between images from two identical scans was used for assessment of noise, were the standard deviation was measured in the area of the measured vein (see method 1 in Table 3). Noise in the magnitude images from the Philips system was measured by repeating the scan with RF turned off (method 2 in Table 3). The noise in the post-processed image was estimated in the same way as for the phantom measurement, see Eq. 23.

In each volunteer, 10 profiles were drawn across veins well-visualized on the post-processed images and subsequently copied to the magnitude images. The contrast was measured in the images as in Figure 12 and calculated as in Eq. 18. CNR was then calculated in the different images in the following way:

$$CNR = \frac{Contrast}{image\ noise} \qquad \text{Eq. 26}$$

CNR enhancement was then calculated in the following way:

$$CNR\ enhancement = \frac{CNR_{Post-processed} - CNR_{Magnitude}}{CNR_{Magnitude}} \qquad \text{Eq. 27}$$

An independent sample t-test was used to compare the degree of contrast enhancement between PADRE and SWI.

**Voxel aspect ratio in sagittal images**

When acquiring sagittal SWI images the effect of the compartment model inside the voxels is different than for transversal images. For in-plane veins perpendicular to the main magnetic field the resultant phase will theoretically be positive (according to Eq. 14 and Eq. 5) in the voxels representing the veins if the regular voxel aspect ratios are used. In this case the negative phase mask will not be able to enhance contrast for sagittal images.

To investigate the relationship between voxel aspect ratio and vein contrast in sagittal images the voxel sizes were varied on the Siemens MR system as well as on the Philips MR system. The sequences in Table 1 were used at respective MR system, but the resolutions used are displayed in Table 5. The contrast enhancement was calculated according to Eq. 19.

**Table 5.** Pulse sequences and resolutions used for investigating contrast enhancement dependence on voxel aspect ratios in sagittal images. For sagittal images is the RL length of the voxel the same as the slice thickness.

| ***MR system*** | ***Pulse sequence*** | ***Resolution*** *(HFxAPxRL)* |
|---|---|---|
| Siemens | 3D GRE | 0.9x0.9x1.5 mm$^3$ |
| Siemens | 3D GRE | 0.8x1.6x0.8 mm$^3$ |
| Siemens | 3D GRE | 1.6x0.8x0.8 mm$^3$ |
| Philips | 3D PRESTO | 1.0x1.0x0.8 mm$^3$ |
| Philips | 3D PRESTO | 1.0x2.0x0.8 mm$^3$ |
| Philips | 3D PRESTO | 2.0x1.0x0.8 mm$^3$ |

Siemens images were post-processed with regular SWI post-processing and with the MATLAB SWI program, where images were processed with both the positive and negative phase masks. On the Philips images, PADRE post-processing was done with VE and TE mode. The filter size used in the MATLAB SWI processing was 128x128 and the number of phase mask multiplications were $m$ = 4. The contrast in five different vessels was measured in the magnitude images and in the post-processed images. Different angled veins were measured: vessel 1 was oriented in the HF direction *i.e.* approximately parallel to

magnetic field, vessel 2 was oriented in the AP direction *i.e.* approximately perpendicular to the magnetic field, the other vessels were directed in oblique directions.

## *Patient images*

During this project, PADRE was used in connection to some patient examinations. There was only one patient that was examined at both Siemens and Philips with the SWI and PADRE sequences respectively.

# Results

## *Phantom experiments*

**Phase mask dependence**

In Figure 14 - Figure 17, magnitude and SWI post-processed images of phantom 1 with cylinders of different sizes are shown. Figure 14 shows images acquired at the Siemens MR camera with cylinders parallel to the magnetic field and Figure 15 shows data acquired at the Siemens camera with cylinders positioned perpendicular to the field. Figure 16 shows images of cylinders parallel to the static magnetic field acquired at the Philips MR system and Figure 17 shows images of cylinders perpendicular to the magnetic field, also acquired at the Philips camera. Magnitude images (a) and post-processed images generated with positive (b) and negative (c) phase masks are displayed. Intensity profiles for lines drawn across the smallest cylinder for the magnitude image (d), for the SWI generated with the negative phase mask (e) and for the SWI generated with the positive phase mask (f) are shown.

The intensity profiles show a signal drop inside the smallest cylinder for the post-processed images, compared to the magnitude images, when using the positive phase mask on the parallel cylinders (Figure 14 and Figure 16) and negative phase masks on the perpendicular cylinders (Figure 15 and Figure 17).

Note that the y-axes are different for the Siemens and the Philips sequences.

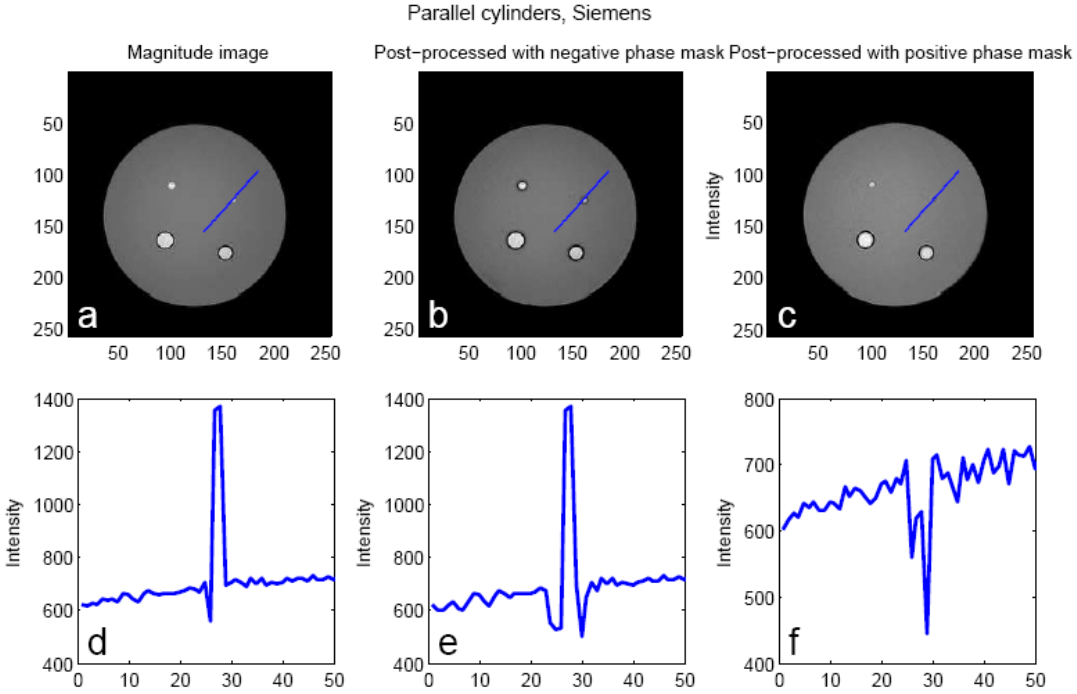


**Figure 14.** MR images of phantom 1 acquired on the Siemens MR system. The cylinders are parallel to the static magnetic field. The upper panel show magnitude (a) and SWI images, generated with the MATLAB SWI program using negative (b) and positive (c) phase mask. The lower panel show profiles over the smallest cylinder are plotted for the magnitude image (d), the SWI image generated with a negative phase mask (e) and the SWI image generated with a positive phase mask (f). Here the positive phase mask generates a signal drop in the post-processed image.

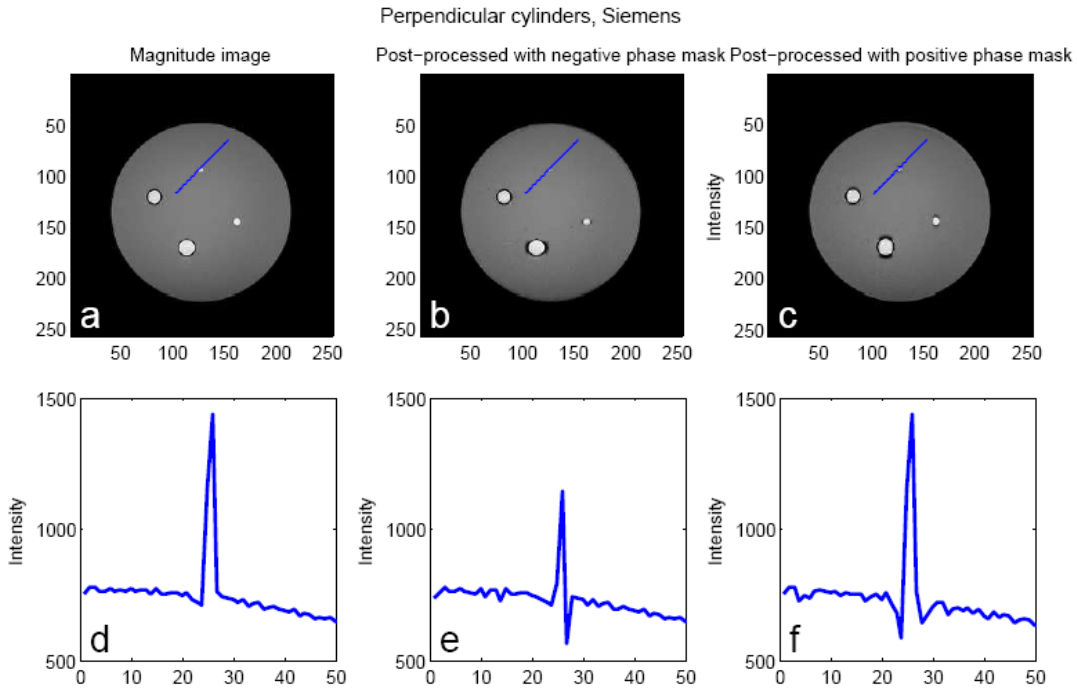


**Figure 15.** MR images of phantom 1 acquired on the Siemens MR system with the cylinders perpendicular to the static magnetic field. The upper panel show magnitude (a) and MATLAB SWI images, generated with negative (b) and positive (c) phase mask. The lower panel show profiles over the smallest cylinder plotted for the magnitude image (d), the SWI image generated with negative phase mask (e) and the SWI image generated with the positive phase mask (f). The negative phase mask causes a signal drop in the post-processed image.

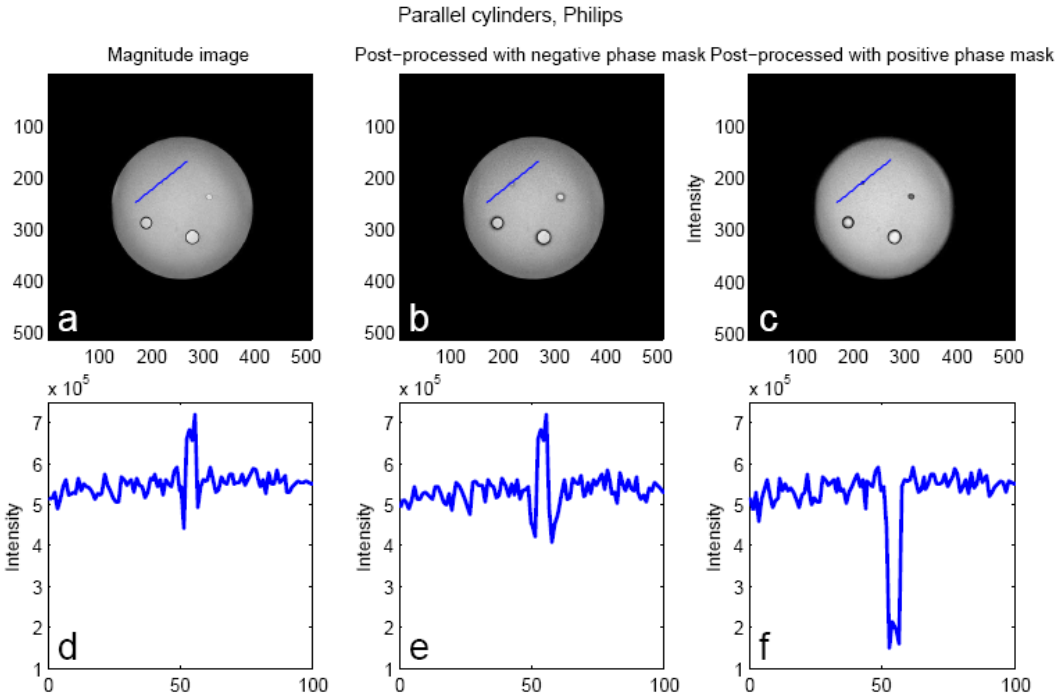


**Figure 16.** Magnitude (a) and post-processed images of phantom 1 with cylinders parallel to the magnetic field acquired at the Philips MR system. SWI was generated in MATLAB with negative (b) and positive (c) phase masks. In the lower panel intensity profiles are plotted for respective image: magnitude image profile (d), profile of SWI generated with the negative phase mask (e) and profile of SWI generated with the positive phase mask (f). The positive phase mask causes a signal drop in the post-processed image (f).

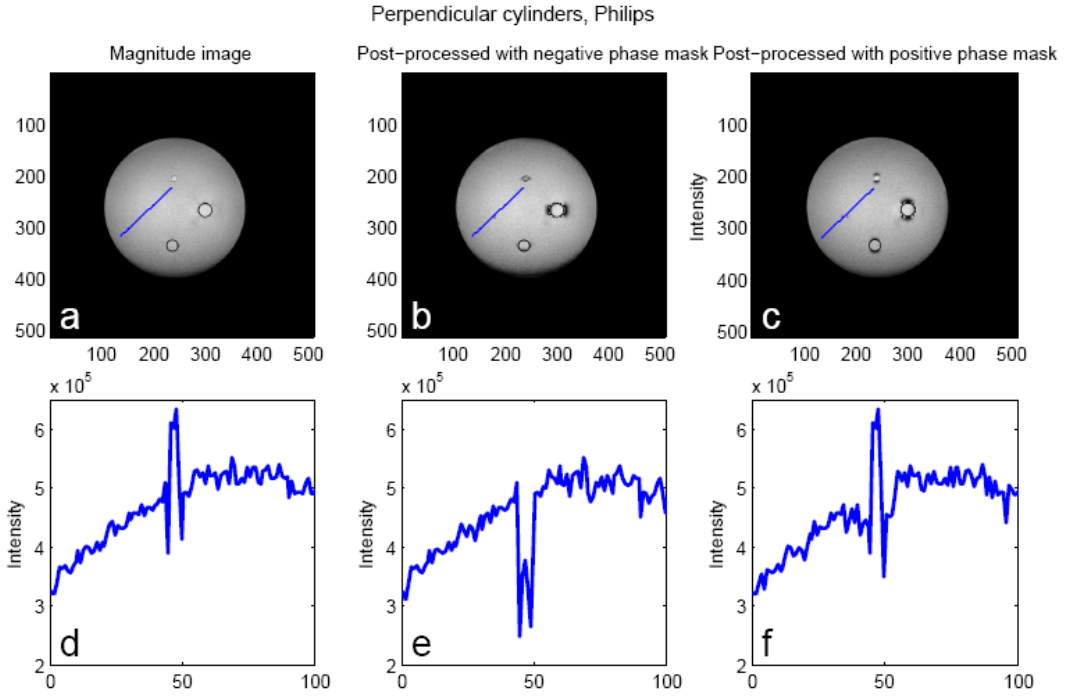


**Figure 17.** Magnitude (a) and post-processed images of phantom 1 with cylinders perpendicular to the static magnetic field during acquisition on the Philips MR system. SWI were generated with negative (b) and positive (c) phase masks. In the lower panel intensity profiles are plotted for respective image: magnitude image profile (d), profile of SWI generated with the negative phase mask (e) and profile of SWI generated with the positive phase mask (f). The negative phase mask causes a signal drop in the post-processed image (e).

**Contrast as a function of filter size**

Figure 18 shows the contrast enhancement of the four cylinders in phantom 1 after MATLAB SWI post-processing. The contrast enhancement is shown as a function of the filter size used for filtering the phase images. Results for three different cylinder angles against the $B_0$ are shown: parallel cylinders, post-processed with positive phase mask (Figure 18a), perpendicular cylinders, post-processed with negative phase mask (Figure 18b), and 55° angled cylinders, post-processed with positive (Figure 18c) and negative (Figure 18d) phase masks. The data is only acquired at the Philips scanner.

Maximal contrast enhancement for most of the graphs is achieved with a filter size of approximately 32x32. Larger filter sizes generate a decrease in contrast enhancement for all cylinders.

The largest cylinders show higher sensitive to filter sizes as the contrast enhancement decreases faster with increasing filter sizes. The smallest cylinder shows a lower contrast enhancement then the others when the filter sizes are small.

The theoretical contrast enhancement for the 55° angled cylinders is zero. However, the results from the SWI generated with the negative phase mask show a small contrast enhancement in all the cylinders.

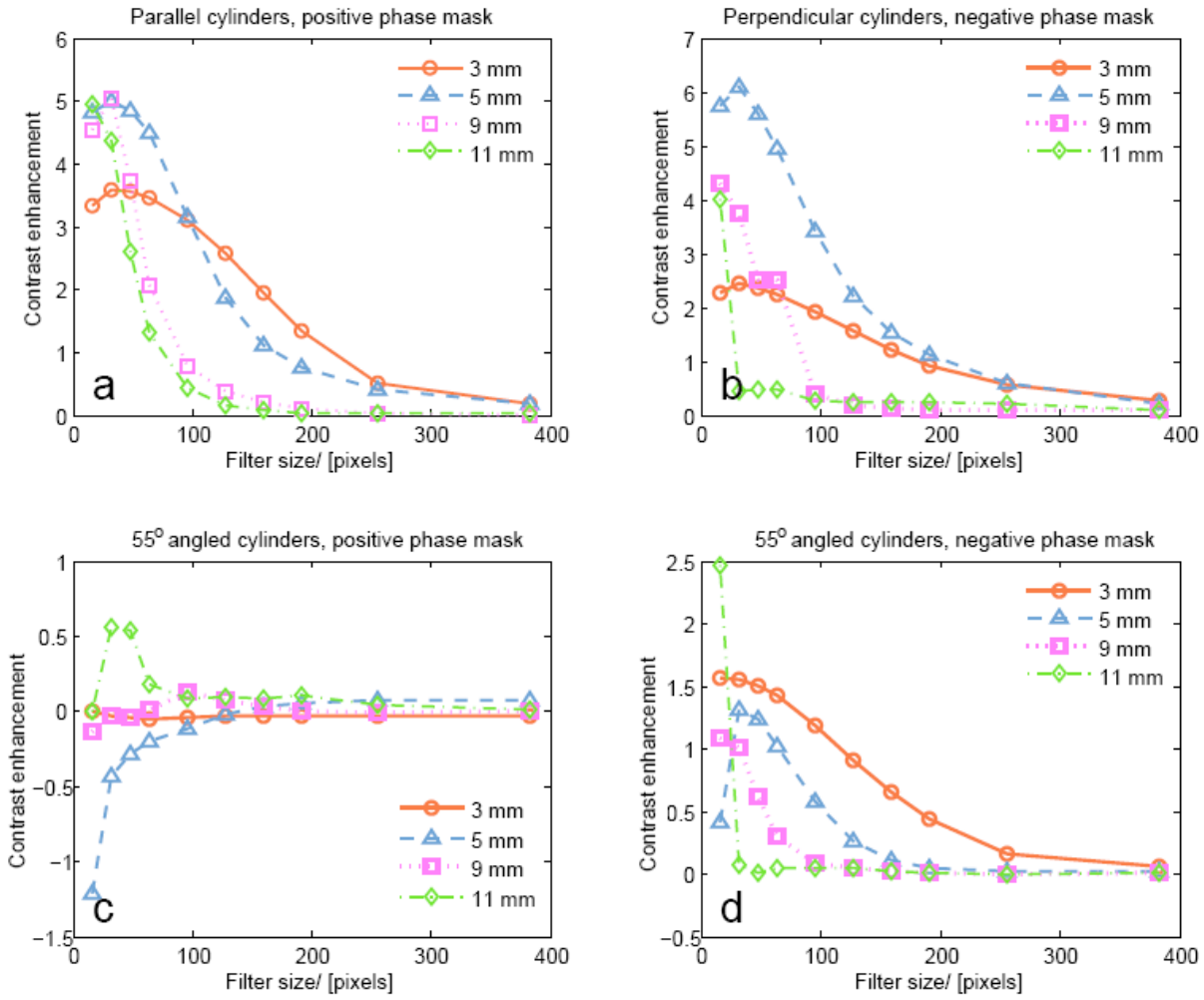


**Figure 18.** Measured contrast enhancement as a function of filter size after MATLAB SWI post-processing for different cylinder sizes positioned with three different angles against the static magnetic field. (a) shows contrast enhancement for cylinders parallel to $B_0$, (b) shows the contrast enhancement for cylinders perpendicular to $B_0$, (c) and (d) shows cylinders angled 55° against $B_0$, where post-processing was performed with the positive and negative phase masks respectively. The acquired phase images had a matrix of 512x512.

**Contrast as a function of cylinder size**

In Figure 19 - Figure 21, contrast enhancement calculated according to Eq. 19 for different pulse sequences, resolutions and post-processing methods are shown for all the cylinder sizes in phantom 1. Pulse sequences and resolutions from Table 2 are used. SWI processing as implemented by the vendor are shown for the Siemens sequence, and all PADRE post-processing modes are shown for the Philips sequences.

Some bars in the plots, show no contrast enhancement at all. This is to be expected when the wrong type of phase mask has been used to generate the post-processed images. For the parallel cylinders, TE mode shows no contrast enhancement, and for perpendicular cylinders, VE mode and SWI show no contrast enhancement. The Padre mode gives contrast enhancement for both directions because it is a combination of both the VE and TE mode. This is most evident when observing the result for the 9 mm cylinder parallel to the magnetic field (Figure 19) which shows a negative contrast enhancement for the TE mode and a positive contrast enhancement for the VE mode. The Padre mode gives a summarized contrast enhancement of the VE and TE mode.

The highest contrast enhancement is achieved for the PRESTO sequence with the resolution recommended by Philips. The bar plot also shows that the PRESTO sequence gives higher contrast enhancement than the GRE sequence when using the same resolution. Furthermore, the Philips GRE sequences post-processed with the PADRE or VE mode give higher contrast enhancement than the Siemens GRE sequence post-processed with SWI for the two smaller cylinders while the SWI on the Siemens GRE gives higher contrast enhancement on the two larger cylinders.

Theoretically there should be no contrast enhancement for the 55° angled cylinders, still this is seen for some sequences.

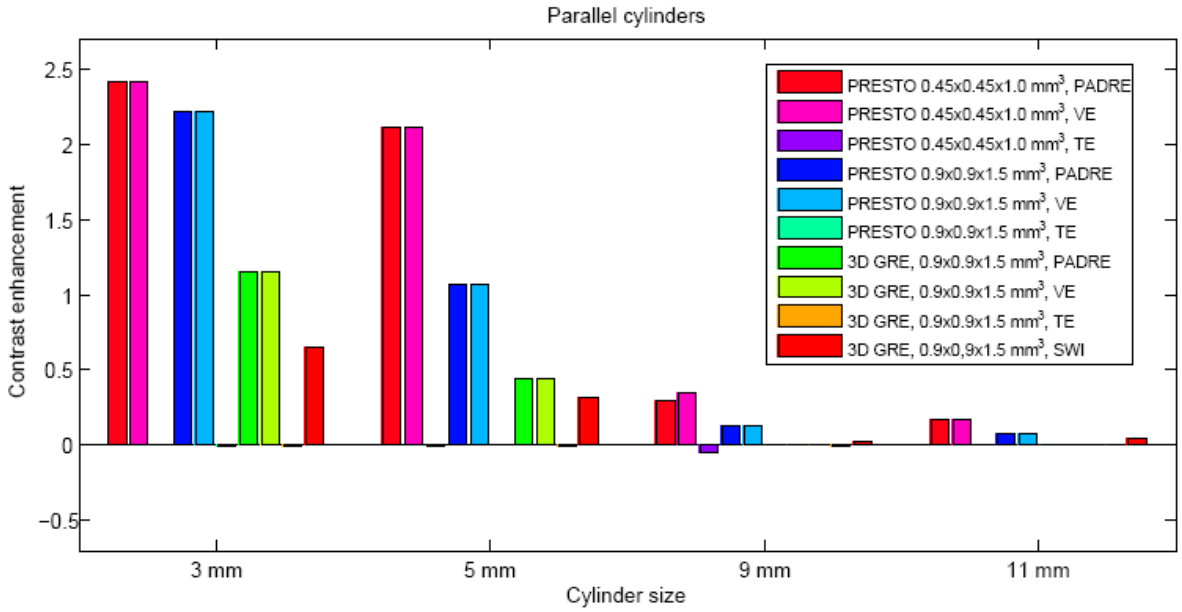


**Figure 19.** Contrast enhancement after post-processing for cylinders of four different diameters, parallel to the main magnetic field. Results from different pulse sequences, resolutions and post-processings are shown. The TE post-processing mode gives no contrast enhancement at this angle.

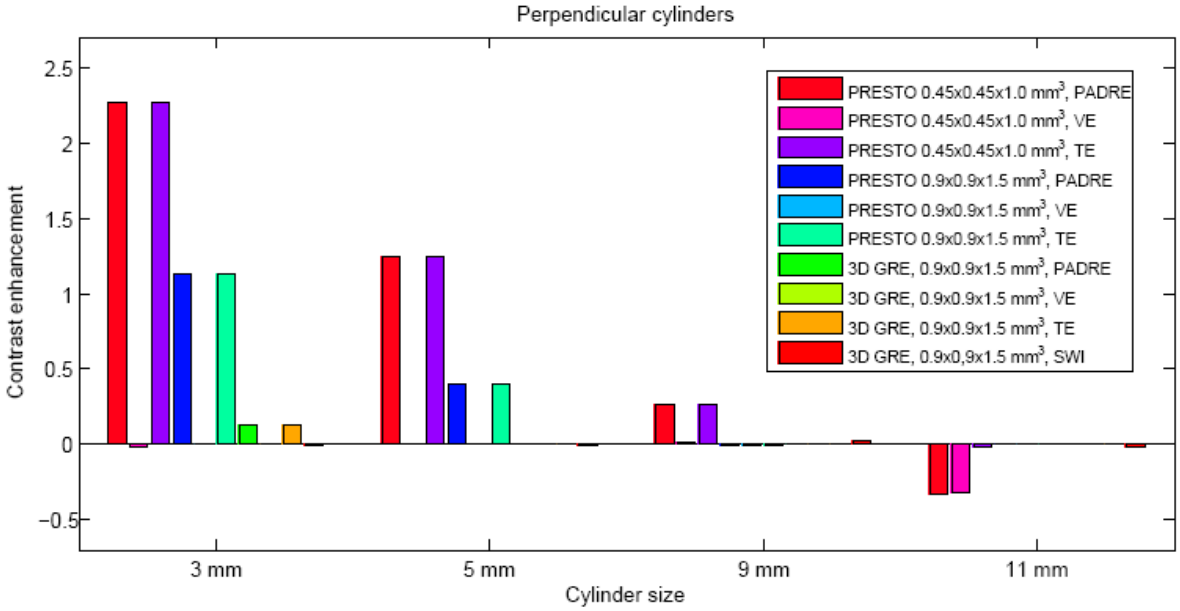


**Figure 20.** Contrast enhancement after post-processing for cylinders of four different diameters, perpendicular to $B_0$. Contrast enhancement for different pulse sequences, resolutions and post-processings are shown. The VE post-processing mode and the SWI post-processing gives no contrast enhancement at this angle.

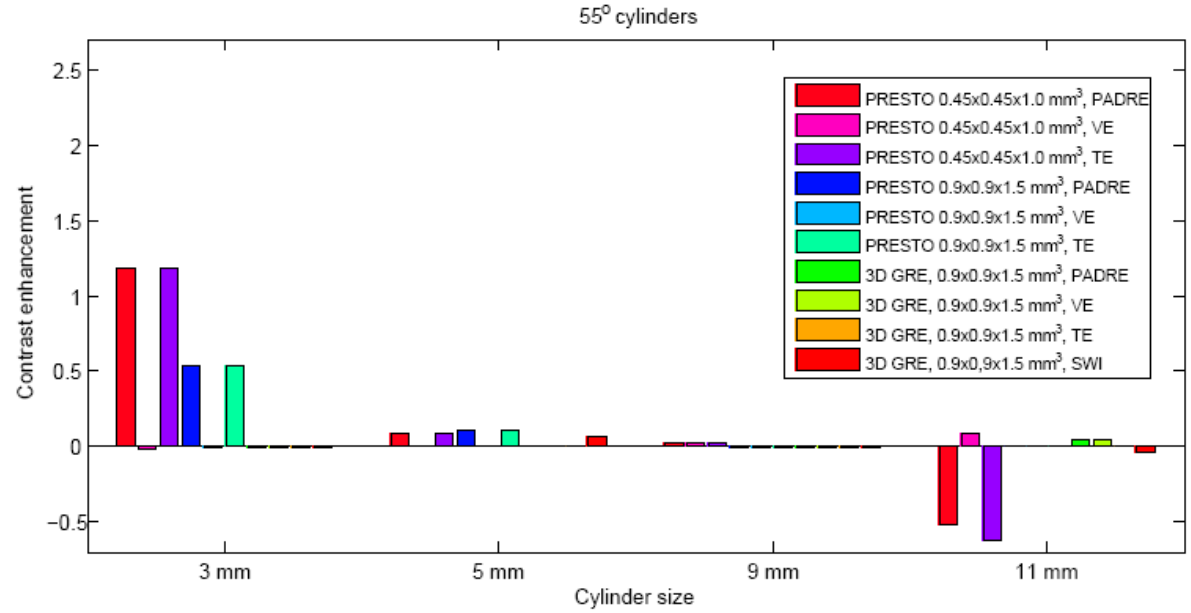


**Figure 21.** Contrast enhancement after post-processing for cylinders of four different diameters, angled 55° to $B_0$. Results from different pulse sequences, resolutions and post-processings are shown. The theoretical contrast enhancement at this angle is zero. However, TE and Padre post-processing gives some contrast enhancement for the smaller cylinders.

### CNR as a function of *m*

In Figure 22, CNR or rather the contrast difference to noise ratio is shown as a function of how many times the phase mask applied to the original magnitude image during post-processing. The plot shows CNR for both Siemens and Philips. The sequences used are according to Table 1 and the post-processing is done with the MATLAB SWI program. For each sequence two different methods of noise assessment

has been used. The methods used are described in Table 3; method 1 (green diamonds) and method 3 (orange circles) were used for the Siemens sequence. Method 2 (pink squares) and method 3 (blue triangles) were used for the Philips sequence.

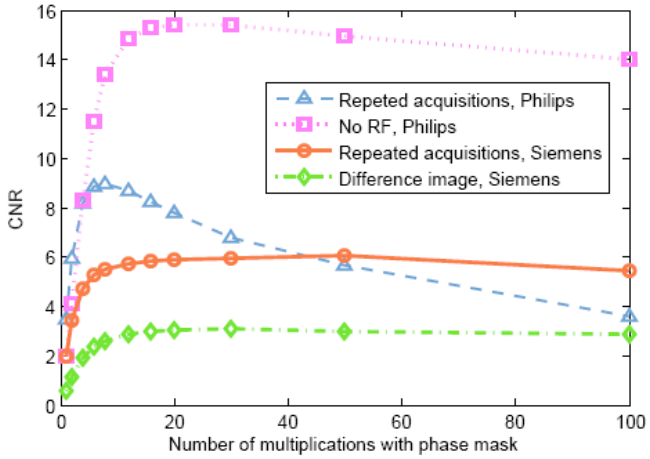


Figure 22. CNR (contrast difference to noise ratio) as a function of the number of times the phase mask has been applied to the magnitude image during post-processing. The different curves show different ways of measuring noise for the Siemens and Philips sequences shown in Table 1.

The two graphs showing the CNR for the Siemens GRE sequence (Diamonds and circles) look very similar but they differ with approximately a factor two. The two graphs showing the CNR for the Philips PRESTO sequence (squares and triangles) are close for a low number of multiplications but diverge increasingly with more multiplications.

When the same noise assessment method is used, the Philips sequence shows a slightly higher contrast difference to noise ratio than the Siemens sequence. The CNR decreases faster for the Philips sequence at higher $m$ than for the Siemens sequence.

## *Volunteer studies*

In Figure 23 below; magnitude-, SWI/PADRE- and minIP of the post-processed images from four different acquisitions of the same volunteer are shown. The sequences used are the ones displayed in Table 2.

The first to columns contain images of the same sequence acquired at the two different MR systems, Siemens (first column) and Philips (second column). The parameters used for acquiring these images were the same so the magnitude images should look the same. However this is not the case, the CSF has higher intensity in the Philips image than in the Siemens image.

All of the post-processed images show higher contrast for veins than the magnitude images and the visualisation of veins increase in the minIP. The Siemens sequence shows a slightly better visualisation of veins for the GRE; especially small veins are more apparent. It appears like the PRESTO sequence gives better visualisation of the veins than the GRE, and the PRESTO sequence with the highest resolution gives the best vein visualization of all sequences.

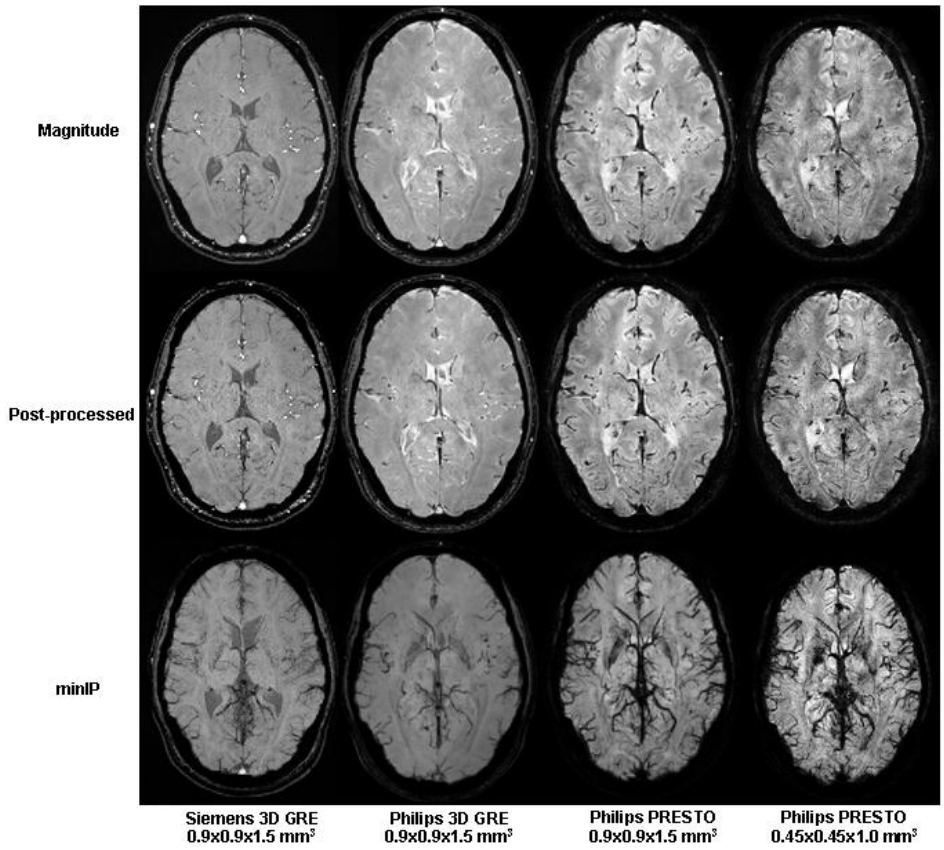


**Figure 23.** Images of one healthy volunteer, acquired with different sequences and resolutions according to Table 2. The top row shows magnitude images from both Siemens and Philips. The images has been post-processed with SWI or PADRE VE respectively (middle row) and finally minIP of the post-processed images has been generated (lower row).

### CNR enhancement measurements

Figure 24 and Figure 25 show how intensity profiles were plotted for lines drawn across a vein in both Siemens images and the Philips images, before and after post-processing. Note that the y-axes are not the same in all the plots. Figure 26 shows the mean CNR enhancement for all 70 veins measured for respective sequence. CNR enhancement for both techniques was approximately 35 %. The result of the independent t-test showed no significant difference between the two CNR enhancement means ($p=0.99$).

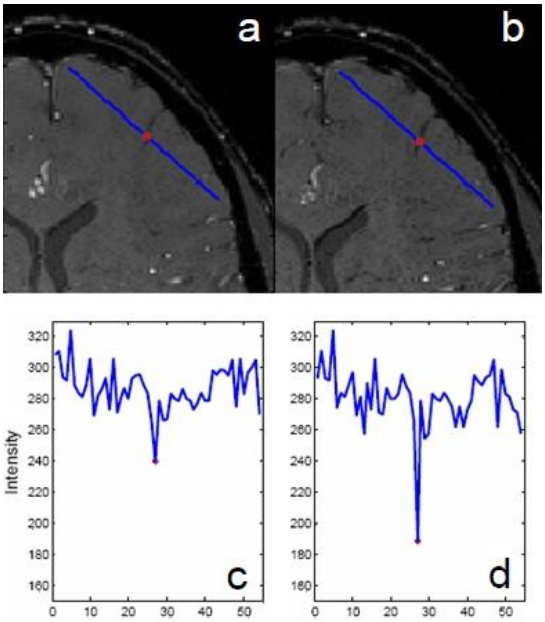


**Figure 24.** Siemens 3D GRE images before and after post-processing with plotted intensity profiles of lines drawn across one vein in respective image. (a) shows magnitude image, (b) shows SWI image, (c) shows intensity profile of line across a vein in the magnitude image and (d) shows intensity profile of line across a vein in the SWI image.

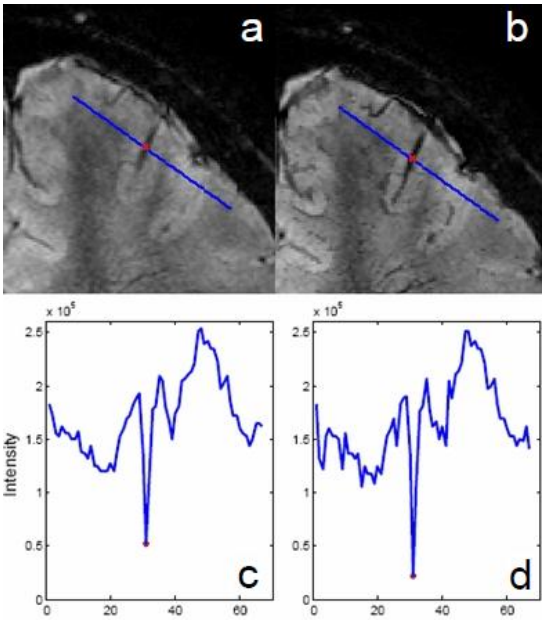


**Figure 25.** Philips PRESTO images before and after post-processing with intensity profiles of lines drawn across a vein. (a) shows magnitude image, (b) shows PADRE VE image, (c) shows intensity profile of line drawn across the vein in the magnitude image and (d) shows the intensity profile of line drawn across a vein in the PADRE image.

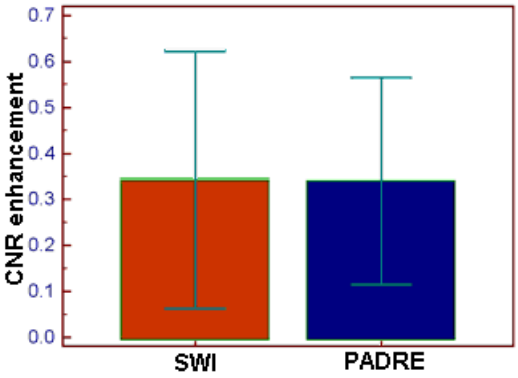


**Figure 26.** Mean CNR enhancement for the two different post-processing techniques SWI and PADRE when using the different pulse sequences and resolutions from respective vendor, shown in Table 1. The left bar shows 34.9 ± 14.0 % CNR enhancement for SWI, and the right bar shows 34.8 ± 11.3 % CNR enhancement for PADRE.

### Voxel aspect ratio in sagittal images

Figure 27 and Figure 28 show relative contrast enhancement for five veins in sagittal images using Siemens SWI and Philips PADRE post-processing respectively, as well as post-processing generated with the MATLAB SWI program. For the Siemens sequence, three post-processings were made: SWI on the camera and also SWI MATLAB program using the positive and the negative phase mask. For the Philips sequence, four post-processings were made: VE, TE, MATLAB SWI generated with the positive phase

mask and MATLAB SWI generated with the negative phase mask. The different plots show the contrast enhancement for the different voxel aspect ratios displayed in Table 5.

It can be seen in the plots that SWI and MATLAB SWI generated with the positive phase mask gives very similar contrast enhancement results. It can also be seen that PADRE post-processing is quite different from the MATLAB SWI. However VE is more like the positive phase mask SWI and TE is more like the negative phase mask SWI for nearly all vessels.

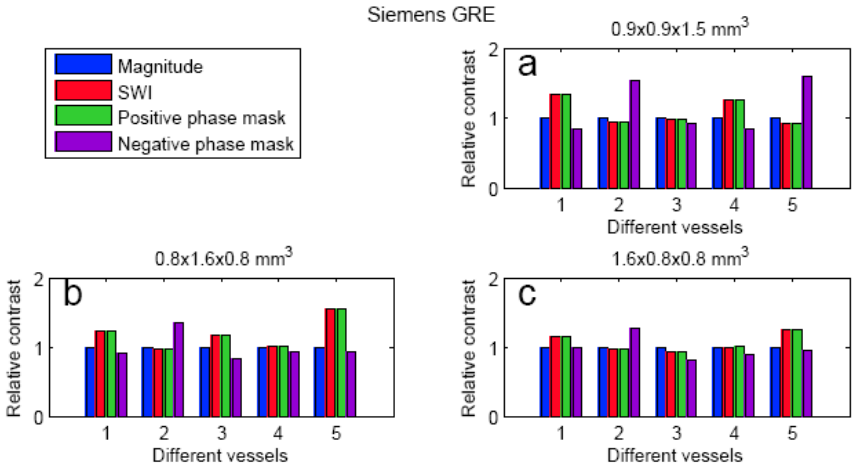


**Figure 27.** Relative contrast for five different vessels in sagittal images acquired with three different AR on the Siemens system with a 3D GRE sequence. The contrast is shown relative to the contrast in the magnitude image (blue bars). The red bars show the SWI from the Siemens system. The green and purple bars shows the contrast for images post-processed in the MATLAB SWI program, generated with the positive and negative phase mask, respectively.

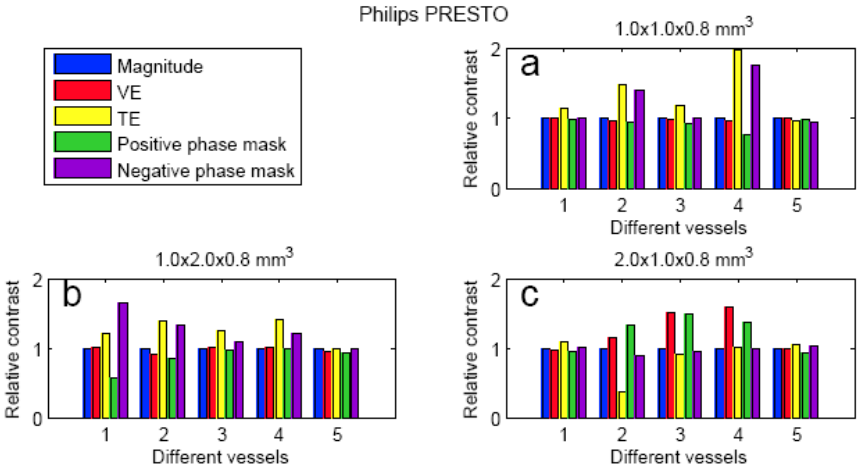


**Figure 28.** Relative contrast for five different vessels in sagittal images acquired with three different AR on the Philips system with a PRESTO sequence. The contrast is shown relative to the contrast in the magnitude image (blue bars). The red and yellow bars show the Vessel Enhancement and Tissue Enhancement contrasts respectively. The green and purple bars shows the contrast for images post-processed in the MATLAB SWI program, generated with the positive and negative phase mask, respectively.

Figure 27a shows the aspect ratio used in the clinic, which is the same aspect ratio that is used for transversal images. Here there is a clear contrast enhancement for the vein perpendicular to the magnetic

field (vessel 2) when using the negative phase mask and not for the SWI post-processing. For the vessel parallel with the magnetic field there is a contrast enhancement with SWI and for the positive phase mask. For Figure 27b and Figure 27c no correlation between the different aspect ratios used and what type of post-processing that generates a contrast enhancement ,can be seen.

In Figure 28a as well as in Figure 28b it can be seen that the TE and the negative phase mask generated MATLAB SWI, gives contrast enhancement for the vein perpendicular to the magnetic field. In Figure 28c it is the VE and the positive phase mask generated MATLAB SWI that gives contrast for the vein perpendicular to the magnetic field.

## *Patient images*

The figure below shows magnitude and post-processed images of a stroke patient, examined at both MR systems with the pulse sequences displayed in Table 1. The post-processed images are SWI and PADRE for Siemens and Philips respectively.

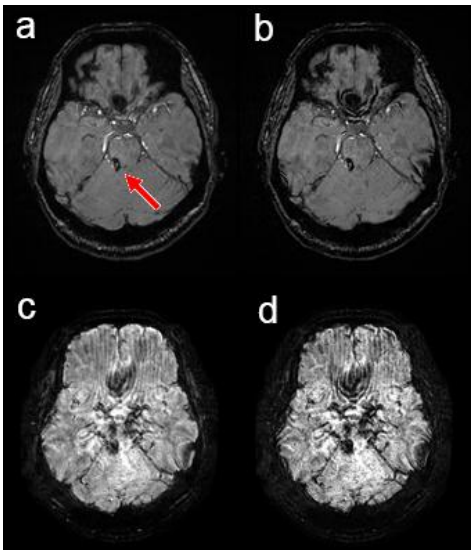


**Figure 29.** Images of a stroke patient examined at both MR cameras. The sequences used are the ones displayed in Table 1. The hemorrhage is shown with a red arrow in (a). The upper row shows images from Siemens: magnitude image (a) and SWI image (b). The lower row shows images acquired at Philips: (c) magnitude image and (d) PADRE image.

The hemorrhage (marked with an arrow in the upper left image) is visible in all images. However, the Philips PRESTO sequence shows much more susceptibility artifacts than the Siemens GRE sequence.

# Discussion

## *Phantom experiments*

The results shown in Figure 14 - Figure 17 are not in agreement with the theoretical phase shift signs that stem from Eq. 13 and Eq. 5. The reason for this is that the Philips and Siemens MR systems that has been used in this work, use a rotating framework for describing the phase (see Appendix for more explanation) instead of the Argand diagram framework, which is used in Eq. 5 [27]. Basically the difference is that the minus sign in Eq. 5 should be taken away when talking about the phase shift at the MR systems used in this work.

There is a difference in signal appearance between the two different MR systems (when comparing for example Figure 14 and Figure 16) because of the different pulse sequences used: the gradient echo on the Siemens system and PRESTO on the Philips system. For both sequences, the signal from the gel inside the cylinders is higher than from the outside gel. The reason for this is that the gadolinium-based contrast agent used to increase the susceptibility inside the cylinders also reduces $T_1$ and thus increasing the magnitude of the signal at the time of the acquisition. After post-processing the signal intensity inside the cylinders are still higher than the outside gel for the Siemens sequence.

The result in Figure 18 shows an optimum filter size of approximately 32x32 which corresponds to the result of Wang *et al.* that got rid of the low spatial field inhomogeneities with the 32x32 Hanning filter [8]. When the filter size increases the contrast enhancement decreases because low frequency variations in phase are being filtrated away. This gives a type of smoothing effect on the images and the contrast will decrease. For the largest cylinder with a diameter of 11 mm (marked with diamonds) the contrast enhancement drops fast to zero because the spatial frequency of the large cylinder will not pass through the high pass filtration at larger filter sizes. The smallest cylinder (marked with circles) shows a lower contrast enhancement than all the other cylinder sizes at small filter sizes when the cylinders are directed parallel and perpendicular to the magnetic field shown in Figure 18a and Figure 18b. According to Eq. 13 the field shifts inside the cylinders are not size dependent and thus the phase inside all the cylinders should be the same. One explanation for the lower contrast enhancement for the smallest cylinder could be that the angle of the cylinder diverges from 0° a little, and thus have a larger angle against the static magnetic field inside the camera during acquisition with parallel cylinders and smaller angle against the field during acquisition with perpendicular cylinders, resulting in a smaller field shift. This can also explain that the smallest cylinder has the largest contrast enhancement at 55°, Figure 18d, when it theoretically should be zero.

There is a small decrease in contrast when going from the second smallest filter size to the smallest filter size. The reason for this is that the smallest filter size cannot remove all the phases outside of the cylinder, caused by low frequency inhomogenities in the magnetic field. In Figure 18c and Figure 18d the theoretical contrast enhancement should be zero which is not the case for the images generated with the negative phase mask. These results indicate, as said earlier, that the angle during acquisition was slightly higher than the magic angle at 55°. In images generated with the positive phase mask (Figure 18c) the contrast enhancement is negative for the second smallest vessel (marked with triangles) at smaller filter sizes because of remaining phase inhomogentities in the outside gel after filtration, leading to lower intensity in the outside gel in the post-processed image than in the magnitude image.

The bar plots in Figure 19 - Figure 21 show a decreasing contrast enhancement for larger cylinder sizes due to the filtration during the post-processing. When comparing to the results in Figure 18 one can assume that the smallest cylinder was better aligned with the magnetic field in this experiment.

Theoretically there should be no contrast enhancement for the 55° angled cylinders; still this is seen for some sequences post processed with TE mode and Padre mode. This correlates to the result in Figure 18d. The negative contrast enhancement for the largest cylinder in both Figure 20 and Figure 21 for the PRESTO sequence could be due to field distortions outside of the cylinder that were included in the intensity profile.

When comparing the results in Figure 19 and Figure 20 with the results in Figure 14 - Figure 17 it is clear that VE and SWI post-processing has the same effect on the contrast as the post-processing done in the MATLAB SWI program using the positive phase mask. In the same way it is clear that TE has the same effect as the MATLAB post-processed images generated with the negative phase mask.

The reason for the difference between the two Siemens CNR graphs in Figure 22 could be due to that the noise measuring method 1 overestimates the noise a little. There can also be a difference in where the profile line was drawn in the image during the contrast analysis. The sensitivity to were and how exactly the profile is drawn, across the cylinder, could be a problem when comparing the two systems with each other. The reproducibility of the method should be looked into. If it turns out that the method is unstable it would require that the phantoms were aligned and turned exactly the same during the two acquisitions in the different scanner. Otherwise one have to look into a more reproducible method of measuring the contrast. The increasing divergence between the two Philip CNR graphs cannot be explained with just a difference in profile location, but rather that there must be an underestimation of the noise with the *no RF* method. It seems that the noise underestimation gets bigger with increasing number of multiplications. For lower $m$, the two graphs seem to follow each other quite well.

The shapes of the CNR curves in Figure 22 look quite similar to the results of Haacke *et al.* [2] for theoretical and simulated CNR as a function the number of multiplications. One difference is that the CNR for the Siemens sequence does not decrease very much at higher $m$. The reason for this is probably that the signal inside the cylinders in the magnitude images are much higher than the outside gel signal (see Figure 14 and Figure 15) this means that it takes much more than a hundred mask multiplications to completely remove the signal inside the cylinders.

## Volunteer studies

In Figure 23 the image result from the four different sequences are displayed in a four times four image matrix. In the first two columns, the GRE sequences from each of the MR systems are displayed. These are acquired with the same parameters and resolution (see the Siemens sequence in Table 1). However, there is a deviation in signal intensity for the CSF (cerebrospinal fluid). I do not know where this deviation in contrast for the CSF comes from. One difference between the two measurements is the number of coil elements used. This would affect the signal intensity overall but should not have an effect on the contrast. The reason for the contrast difference for the two GRE sequences should be looked into further.

When comparing the PRESTO sequence images with the GRE sequence images from the Siemens system, there is a higher signal for the CSF in the PRESTO images as well as higher contrast between grey and white brain matter, which could be due to differences in echo times and flip angles between the two sequences.

The difference in signal between the two 3D GRE sequences shown in Figure 23, might be a reason for some of the contrast enhancement differences shown between the two sequences in Figure 19- Figure 21. To evaluate the difference in post-processing techniques the sequences used should be as equal as possible.

The profile lines shown in Figure 24 and Figure 25 are drawn across the same vein in the same volunteer but this was not done systematically during the analysis as it was difficult to find the exact same vein in both series, due to the fact that the slices were not rotated exactly the same amount, and they did not have the same thickness. Both techniques show signal reduction in veins after post-processing. The results show that there is no significant difference between the contrast enhancements for the two techniques. The methods used for assessment of noise were used for the phantom study as well, see Figure 22. The underestimation of the noise for method 2 seems to be smaller for lower *m*. There is no information of how many multiplications with the phase mask that is done in PADRE but it would be reasonable to believe that it is approximately four as for SWI. If the noise in the PADRE volunteer images is underestimated and therefore actually is higher than the one used to calculate CNR enhancement, then the real PADRE bar shown in Figure 26 should be somewhat lower. The best way to measure the absolute CNR in volunteers would be to assess noise with the *repeated acquisition* method.

The results in Figure 27 and Figure 28 shows that SWI and MATLAB SWI generated with the positive phase mask gives very similar contrast enhancement results. This indicates that the MATLAB SWI program has a good conformity to the SWI used by Siemens, keeping in mind that no filtration was needed for the Siemens phase images. To investigate how good conformity the MATLAB SWI program has to general SWI, unfiltered phase images should be withdrawn from the Siemens camera. The PADRE post-processing is more different from the MATLAB SWI post-processing. However it is not clear where the difference lie; it could be differences in either the phase filtering, in the phase mask generating and/or in the phase mask multiplication.

The bar plot showing the contrast enhancement for the resolution used in the clinic for sagittal images (Figure 27a) show that the SWI post-processing does not always give the best contrast enhancement, especially not for vessels perpendicular to the magnetic field. The reason for this is that the voxel includes the phase signs perpendicular to the magnetic field instead of parallel to the magnetic field (see Figure 4). There is almost no difference between the different aspect ratios used for the Siemens sequence. Theoretically it should be a difference for AR = 1:2:1 and 2:1:1 but there is none. However there is a difference between the different aspect ratios in the Philips images. For the perpendicular vein there is a contrast enhancement when using the negative phase mask for the 1.0x1x0x0.8 $mm^3$ resolution as well as for the 1.0x2x0x0.8 $mm^3$ resolution. For the 2.0x1x0x0.8 $mm^3$ resolution there is a contrast enhancement when using the positive phase mask. These results are in agreement with the theory.

## *Patient images*

The images in Figure 29 show the only patient who was examined at both MR systems during this project. They show a hemorrhage before and after post-processing. The visual difference between the magnitude and the post-processed images are greater for the PRESTO sequence. The hemorrhage seems a bit wider but there are also more artifacts in the PADRE image than in the magnitude image. The hemorrhage is located far down in the brain, close to air cavities which causes the artifacts. These artifacts are larger for the PRESTO sequence since $T_E$ is longer. This far down in the brain, there can also be a problem with a lot of phase wraps, which cannot be removed during filtration.

The selection of this patient was not randomized since the patient was examined at the Siemens system first and later sent to the Philips system because of the nice image.

## Methods

The phantoms that were made and used in this project were handy to use but the agar-gels could have been optimized to resemble the signal appearance of blood vessels better. The present phantoms are not well suited for comparing with in-vivo studies since the signal inside the cylinders are higher than the signal outside of the cylinders, making absolute CNR measurements before and after post-processing useless. Therefore the *contrast difference* before and after the post-processing was calculated and normalized to the noise measured in the post-processed image.

The contrast measurements done in this project, involved a line drawn across the cylinder or vein that was used to plot an intensity profile. To get better statistics for the intensity of the veins, larger ROIs including more pixels should be defined inside the vessels. This could maybe be done by segmenting the veins in minIP images.

The reason for using the different methods for assessment of noise was that the difference image calculated from two acquisitions on the Philips system included a lot of tissue signal instead of only the subtracted noise. A reason for this could be RF-instability. On the Siemens system, method 2 was not used, since the knowledge of how to turn off the RF was lacking at the time of the experiments.

The three different noise estimations use different sources for describing the image noise. In both the first and the second method, the spatial signal variation is considered to be the noise in the image and is measured within a ROI. Both methods include thermal noise from the measured object but also from thermal noise in the electronics. The first method however also includes system noise proportional to the signal, *e.g.* from RF-instability. According to Yu *et al.* [26], the thermal noise variance is the same in data acquisitions with and without RF excitation, provided that all other parameters of the acquisitions stay the same, the second method only includes thermal noise from the object and the electronics. In the third noise assessment method, identical acquisitions were made repeatedly 20 times so there will be an additional noise measured in this method, *i.e.* the physical noise.

Different sources of error occur when using the different noise assessment methods used in this work. Both method 1 and method 2 requires the noise to be homogenous within the ROI where the signal is measured. This is not always the case when using parallel imaging [28]. However, it has been verified that method 2 at the Philips scanner gives a noise image without influence of parallel imaging, even when SENSE is used [Dr. Cecilia Pozzanzini, Philips, personal communication]. To be able to use method 2 correctly, all the reconstruction and post-processing steps must be known and there are many technical difficulties involved in this method [28]. In the third method, the noise is only measured in one voxel and thus it does not have the same requirements of homogenous noise distribution. However, method 3 requires that the acquisition set-up is the same in all the repetitions and that the subject does not move. This is easy to achieve in a phantom measurement but it can be difficult for a volunteer to lie completely still for the entire time, especially if there are many repetitions.

In the volunteer study, two different methods of noise assessment were used for the two different MR systems. Since all the methods include different sources of noise it would be preferred to use the same method, preferably the *repeated acquisitions* method (method 3), but this takes a lot of scanning time. It would be possible to use the *no RF excitation* method (method 2) if all the steps of the PADRE post-processing was known. Then, the noise in the post-processed images could be calculated numerically,

which has been shown for SWI by Haacke *et al.* [2]. The *difference image* (method 1) might be possible to use, but then the signal in the two acquisitions has to be the same, for example the RF should be more stable.

The method of estimating the noise, done in this work, according to Eq. 23, underestimates the noise. Furthermore, the different noise measurements, for the two different systems, make it difficult to compare the two systems with each other. This is a limitation of the volunteer study. However, all the three methods are used in the phantom study which makes it possible to calibrate method 1 and method 2 with method 3.

The voxel aspect ratio experiment in this work was just a pilot test to see if the theory of the compartment model inside the voxels could have an effect on post-processed sagittal images. To better show the relationship between voxel aspect ratios and contrast enhancement, more vessels should be measured. It would also be interesting to see how the angle dependence of the vessels contributes to the contrast enhancement.

To better compare the two MR systems the pulse sequences used should be as identical as possible, while we in this study used the default sequence on the Siemens system and the vendor-recommended sequences on the Philips system. Preferably, the subjects measured at the two-different cameras should have the head in the exact same position during the two occasions. This can be difficult to accomplish; one way could be to create a special neck cushion that can be used in both of the cameras.

A visual comparison by radiologists was not made in this work. The reason for this is that a diagnostic quality of the images could not be determined since only one patient was measured at both systems. However, overall image quality could have been established by radiologists also for volunteer data but for this it would be preferred that the observers where blinded, and there was no time for such set-up during this work. A larger scale visual grading of the two techniques is planned for patients with cerebral hemorrhages.

# Conclusions

The studies in this work have shown that there are differences between the SWI and PADRE implementations that affect the contrast enhancement after post-processing. The SWI post-processing has shown to be very similar to the MATLAB SWI program made in this project. The PADRE post-processing on the other hand is somewhat different to the MATLAB SWI program. It has also been shown that the PADRE post-processing mode is the same as adding tissue enhancement and vessel enhancement modes together. The Padre mode might have advantages for contrast enhancement when several angles exists in the same object.

When observing minIPs of the SWI and PADRE images generated from the different pulse sequences shown in Table 1, there is visually a difference in venous contrast. However no significant difference between the two sequences and post-processing techniques could be shown when measuring contrast difference to noise ratio in a large number of veins in healthy volunteers. When using the 3D gradient echo on both systems with the same resolution, SWI appeared to give a better visualization of veins, especially small ones, but this has yet to be quantified. The PRESTO sequence shows a lot of susceptibility artefacts in the lower parts of the brain which might limit the clinical use of this sequence.

The phantom studies of this work has shown how the angle of cylinders affect the contrast enhancement in the post-processed images depending on which phase mask is used. The CNR measurement as a function of the number of phase masks applied to the magnitude image, using different

methods of noise assessment show very varying results, especially for the ones used on the PADRE images. The method using no RF excitation for assessment of noise, severely underestimates the noise in the post-processed image. To use this technique successfully, one has to know all the post-processing steps of PADRE and calculate its influence of the noise.

## Future work

Approval for studies of different patient groups has been received from the local ethics committee and as a continuation of the work presented here, a group of stroke patients will be examined with both SWI on the Siemens MR and PADRE on the Philips system during the fall of 2011. In order to compare post-processing techniques, imaging sequences will be harmonized as much as possible. The results will be analyzed both quantitatively (SNR, CNR) and qualitatively (diagnostic accuracy, image quality). The same type of study might also be done for other patient groups The images will be qualitatively graded by radiologists.

Further development of the MATLAB SWI program and of the analyze program will be executed to improve the CNR measurements. Absolute CNR measurements will be done for volunteers using the *repeated acquisition* method.

## Acknowledgments

First of all, I would like to thank my supervisor Karin Markenroth for all the encouragement and help that I've received during this project. There have been many scanning hours (and post-processing hours) at the cameras; it has been fun and I've learned a lot. Also, thank you Emelie Lindgren for rewarding discussions about susceptibility and for your collaboration with the phantom making. I would also like to thank Ronnie Wirestam, Jimmy Lätt and Peter Mannfolk and all the other members in the MR physics group here at Lund University, for help and support. Last but not least I would like to thank all the volunteers that have participated in my studies.

# References


1. Sehgal, V., et al., *Clinical applications of neuroimaging with susceptibility-weighted imaging.* Journal of Magnetic Resonance Imaging, 2005. **22**(4): p. 439-450.

2. Haacke, E., et al., *Susceptibility weighted imaging (SWI).* Magnetic Resonance in Medicine, 2004: p. 612-618.

3. Yoneda, T., et al., *High-Contrast Delineation of the Optical Radiation using Phase Difference Enhanced Imaging (PADRE).* 2009: RSNA.

4. Boeckh-Behrens, T., et al., *Susceptibility-weighted angiography (SWAN) of cerebral veins and arteries compared to TOF-MRA.* Eur J Radiol, 2011.

5. Haacke, E.M., et al., *Magnetic Properties of Tissues: Theory and Measurement*, in *Magnetic Resonance Imaging Physical Principles and Sequence Design* 1999, John Wiley & Sons, Inc. p. 741-777.

6. Haacke, E., et al., *Susceptibility-Weighted Imaging: Technical Aspects and Clinical Applications, Part 1.* American Journal of Neuroradiology, 2009: p. 19-30.

7. Schenck, J.F., *The role of magnetic susceptibility in magnetic resonance imaging: MRI magnetic compatibility of the first and second kinds.* Medical Physics, 1996. **23**(6): p. 815-850.

8. Wang, Y., et al., *Artery and vein separation using susceptibility-dependent phase in contrast-enhanced MRA.* J Magn Reson Imaging, 2000. **12**(5): p. 661-70.

9. Spees, W.M., et al., *Water proton MR properties of human blood at 1.5 Tesla: magnetic susceptibility, T(1), T(2), T*(2), and non-Lorentzian signal behavior.* Magn Reson Med, 2001. **45**(4): p. 533-42.

10. Thomas, B., et al., *Clinical applications of susceptibility weighted MR imaging of the brain - a pictorial review.* Neuroradiology, 2008: p. 105-116.

11. Mittal, S., et al., *Susceptibility-Weighted Imaging: Technical Aspects and Clinical Applications, Part 2.* American Journal of Neuroradiology, 2009: p. 232-252.

12. Santhosh, K., et al., *Susceptibility weighted imaging: a new tool in magnetic resonance imaging of stroke.* Clin Radiol, 2009. **64**(1): p. 74-83.

13. Akter, M., et al., *Detection of hemorrhagic hypointense foci in the brain on susceptibility-weighted imaging: Clinical and phantom studies.* Academic Radiology, 2007: p. 1011-1019.

14. Rauscher, A., et al., *Magnetic susceptibility-weighted MR phase imaging of the human brain.* American Journal of Neuroradiology, 2005. **26**(4): p. 736-742.

15. Wikipidia. *Hann function. The Free Encyclopedia* [cited 2011 14 Aug]; Available from: http://en.wikipedia.org/wiki/Hann_function.

16. Denk, C. and A. Rauscher, *Susceptibility weighted imaging with multiple echoes.* J Magn Reson Imaging, 2010. **31**(1): p. 185-91.

17. Xu, Y. and E.M. Haacke, *The role of voxel aspect ratio in determining apparent vascular phase behavior in susceptibility weighted imaging.* Magn Reson Imaging, 2006. **24**(2): p. 155-60.

18. Deistung, A., et al., *Susceptibility weighted imaging at ultra high magnetic field strengths: theoretical considerations and experimental results.* Magn Reson Med, 2008. **60**(5): p. 1155-68.

19. Brainovich, V., U. Sabatini, and G.E. Hagberg, *Advantages of using multiple-echo image combination and asymmetric triangular phase masking in magnetic resonance venography at 3 T*. Magn Reson Imaging, 2009. **27**(1): p. 23-37.

20. Liu, G., et al., *A functional MRI technique combining principles of echo-shifting with a train of observations (PRESTO)*. Magn Reson Med, 1993. **30**(6): p. 764-8.

21. Yoneda, T., et al., *Triple-layer Appearance of Human Cerebral Cortices on Phase-Difference Enhanced Imaging using 3D Principle of Echo Shifting with a Train of Observations (PRESTO) Sequence*. 2009: ISMRM Proceedings of 17th Annual meeting. p. 2764.

22. Moore, L., *Instruction for Use WIP PADRE PRIDE tool R2.6 or higher*. 2010, Philips MR Clinical Science. p. DHF107687/UM.

23. Pruessmann, K.P., et al., *SENSE: sensitivity encoding for fast MRI*. Magn Reson Med, 1999. **42**(5): p. 952-62.

24. Sodickson, D.K., M.A. Griswold, and P.M. Jakob, *SMASH imaging*. Magn Reson Imaging Clin N Am, 1999. **7**(2): p. 237-54, vii-viii.

25. Association, N.E.M., *Determination of signal-to-noise ratio (SNR) in dagnostic magnetic resonance imaging.*, in *NEMA standards Publications MS 1-2008*. 2008, National Electrical Manufacturers Association: Rosslyn.

26. Yu, J., et al., *Practical signal-to-noise ratio quantification for sensitivity encoding: application to coronary MR angiography*. J Magn Reson Imaging, 2011. **33**(6): p. 1330-40.

27. Hagberg, G.E., E.B. Welch, and A. Greiser, *The sign convention for phase values on different vendor systems: definition and implications for susceptibility-weighted imaging*. Magn Reson Imaging, 2010. **28**(2): p. 297-300.

28. Dietrich, O., et al., *Measurement of signal-to-noise ratios in MR images: influence of multichannel coils, parallel imaging, and reconstruction filters*. J Magn Reson Imaging, 2007. **26**(2): p. 375-85.

# Appendix

## *Phase sign convention*

When creating susceptibility weighted images using both magnitude and phase images, it is of outermost importance to understand how the phase is affected by susceptibility variations in tissues. The theoretical shift in the magnetic field around tissues with different susceptibilities and geometries of different orientations are known from the literature but the actual value of the phase will depend on the sum effect of hardware differences in different vendor systems. Ultimately, an MR system uses one out of two different frameworks for describing spin behaviour.

The two different frameworks that will affect the phase sign convention of a system are: either the physical rotating MR frame of reference for representing the Larmor precession of proton spins or the mathematical representation of complex numbers in the Argand diagram.

The rotating frame of reference describes how the spins with magnetic moment $\mu$ are experiencing a torque when placed in a uniform magnetic field, $B_0$. A proton will precess with the Larmor frequency, $\omega_0$, around $B_0$ in a positive direction leading to a clockwise rotation. After a 90° RF pulse applied in the x-direction the spin precession are represented by a vector along the y-axis in a Cartesian 3D space with an x-y plane rotating with $\omega_0$ about the z-axis, representing the direction of the applied magnetic field. Local magnetic susceptibility variation will affect the magnetic field and thus the local Larmor frequencies of the spins. In paramagnetic areas the magnetic field will be increased and so the spins will rotate faster. This will lead to a clockwise movement of the spin in the rotating frame of reference and so the phase shift, $\Delta\varphi$, is considered positive. The opposite will happen in diamagnetic areas where the spins will rotate slower and thus create a negative phase shift.

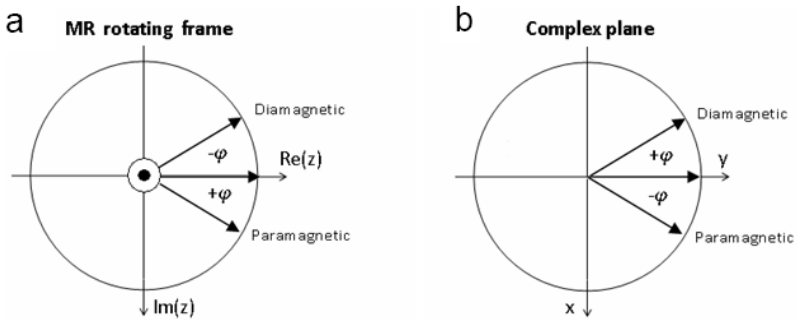


**Figure 30.** The two different frameworks for deciding the phase sign of the MR signal after dephasing in areas with different susceptibility. The left image (a) shows the physical rotating MR frame of reference for representing the spins processing about the magnetic field, $B_0$, with the Larmor frequency. The right image (b) shows the mathematical representation of complex numbers in the Argand diagram. (image borrowed and modified [27])

On the other hand can the MR signal be represented by complex numbers and are described by position vectors in an Argand diagram, where the imaginary part, Im(z), is represented along the vertical axis, and the real part, Re(z), is represented along the horizontal axis, in a 2D complex plane. The phase range in the Argand diagram is either $[-\pi, \pi)$ or $[0, 2\pi)$ and an increase in phase are represented by a counter clockwise rotation about the centre of the complex plain. This gives a negative phase sign for spin dephasing caused by paramagnetic materials.